

1                   **Organization of Peptidoglycan Synthesis in Nodes and Separate Rings at**  
2                   **Different Stages of Cell Division of *Streptococcus pneumoniae***

3  
4                   Amilcar J. Perez<sup>at</sup>, Michael J. Boersma<sup>at</sup>, Kevin E. Bruce<sup>at</sup>, Melissa M. Lamanna<sup>a</sup>,  
5                   Sidney L. Shaw<sup>a</sup>, Ho-Ching T. Tsui<sup>a</sup>, Atsushi Taguchi<sup>b</sup>, Erin E. Carlson<sup>c</sup>, Michael S.  
6                   VanNieuwenhze<sup>d</sup>, and Malcolm E. Winkler<sup>a#</sup>

7  
8                   <sup>a</sup>Department of Biology, Indiana University Bloomington, Bloomington, IN 47405 USA

9                   <sup>b</sup>Department of Microbiology, Harvard Medical School, Boston, MA 02115 USA

10                  <sup>c</sup>Department of Chemistry, University of Minnesota, Minneapolis, MN 55455 USA

11                  <sup>d</sup>Department of Chemistry, Indiana University Bloomington, Bloomington, IN 47405 USA

12  
13                  Running title: Microscopy of Vertically Oriented Pneumococcal Cells

14  
15                  Keywords: septal and peripheral peptidoglycan synthesis; penicillin-binding proteins  
16                  (PBPs); FtsX; fluorescent D-amino acids (FDAAs); high-resolution 3D-SIM

17  
18                  <sup>†</sup>Contributed equally to this work. Author order was determined by random draw.

19                  <sup>#</sup>Corresponding author:

20                  Malcolm E. Winkler  
21                  Department of Biology  
22                  Indiana University Bloomington  
23                  1001 East Third Street  
24                  Bloomington, Indiana USA 47405  
25                  Phone: 812-856-1318  
26                  Email: [winklerm@indiana.edu](mailto:winklerm@indiana.edu)

27 **ABSTRACT**

28 Bacterial peptidoglycan (PG) synthesis requires strict spatial and temporal  
29 organization to reproduce specific cell shapes. In the ovoid-shaped, pathogenic bacterium  
30 *Streptococcus pneumoniae* (*Spn*), septal and peripheral (sidewall-like) PG synthesis  
31 occur simultaneously at midcell. To uncover the organization of proteins and activities  
32 that carry out these two modes of PG synthesis, we examined *Spn* cells vertically oriented  
33 onto their poles to image the division plane at the high lateral resolution of 3D-SIM  
34 (structured-illumination microscopy). Using fluorescent D-amino acid (FDAA) probes, we  
35 show that areas of new transpeptidase (TP) activity catalyzed by penicillin-binding  
36 proteins (PBPs) separate into a pair of concentric rings early in division, representing  
37 peripheral PG (pPG) synthesis (outer ring) and the leading-edge (inner ring) of septal PG  
38 (sPG) synthesis. Fluorescently tagged PBP2x or FtsZ locate primarily to the inner FDAA-  
39 marked ring, whereas PBP2b and FtsX remain in the outer ring, suggesting roles in sPG  
40 or pPG synthesis, respectively. Short pulses of FDAA labeling revealed an arrangement  
41 of separate regularly spaced “nodes” of TP activity around the division site of predivisional  
42 cells. Control experiments in wild-type and mutant strains support the interpretation of  
43 nodal spacing of TP activity, and statistical analysis confirmed that the number of nodes  
44 correlates with different ring diameters. This nodal pattern of FDAA labeling is conserved  
45 in other ovoid-shaped species. Tagged PBP2x, PBP2b, and FtsX proteins also exhibited  
46 nodal patterns with spacing comparable to that of FDAA labeling. Together, these results  
47 reveal a highly ordered PG synthesis apparatus in ovococcal bacteria at different stages  
48 of division.

49 **SIGNIFICANCE**

50 The spatial organization of PBPs and their TP activity at division septa is not well  
51 understood. In some bacteria, TP activity and PBP localization seem to be nodal (also  
52 called punctate), whereas in other bacteria, discrete foci of PBP activity are infrequently  
53 or not observed. Here we report two basic properties of the organization of PBPs and TP  
54 activity in the ovoid-shaped bacterium *Spn*. First, there is distinct spatial separation of the  
55 sPG machine, including FtsZ, from the pPG synthesis machine at the midcell of dividing  
56 *Spn* cells. Second, in predivisional cells, PBPs and TP activity are organized  
57 heterogeneously into regularly spaced nodes, whose number and dynamic distribution  
58 are likely driven by the PG synthesis of PBP:SEDS complexes.

59

60 **INTRODUCTION**

61 *Streptococcus pneumoniae* (pneumococcus; *Spn*) is a Gram-positive, commensal  
62 bacterium of humans and a major opportunistic pathogen that causes life-threatening  
63 illnesses, including pneumonia, bacteremia, and meningitis (1, 2). *Spn* is a prolate  
64 ellipsoid-shaped bacterium, referred to as an ovococcus (3). Its distinct ovoid shape is  
65 maintained by a thick peptidoglycan (PG) wall that surrounds the entire cell (4). PG  
66 consists of glycan sugar chains of alternating units of  $\beta$ -(1,4) linked N-acetylglucosamine  
67 (GlcNAc) and N-acetylmuramic acid (MurNAc). Glycan chains are crosslinked together  
68 by PG peptides attached to MurNAc, thereby forming a mesh-like network (5, 6). As in  
69 most eubacteria, *Spn* PG synthesis is essential for normal growth and cell division and  
70 determines normal cell shape and chaining, which impact colonization and virulence (4,  
71 7, 8). Besides protecting cells from turgor stress, *Spn* PG serves as a scaffold for surface-

72 attached virulence factors, including capsule, sortase-attached proteins, and wall teichoic  
73 acids (4).

74 In *Spn*, PG synthesis is organized initially by an FtsZ ring at the midcell equator  
75 perpendicular to the long axis of newly divided cells (Fig. S1). PG synthesis is carried out  
76 by distinct septal PG (sPG) and peripheral PG (pPG) modes (9-11). sPG synthesis  
77 produces the cross wall that separates daughter cells (12-14), whereas concurrent pPG  
78 synthesis elongates daughter cells from midcell to form ovoid-shaped cells (Fig. S1) (11-14).  
79 pPG synthesis in *Spn* functionally resembles preseptal PG elongation that occurs briefly  
80 at the beginning of division of rod-shaped bacteria (15, 16). However, pPG elongation in  
81 *Spn* cells remains confined to the midcell region, in contrast to lateral PG elongation  
82 organized by MreB-containing Rod complexes moving over the body of rod-shaped cells  
83 (5).

84 The location of these two modes of PG synthesis within the same midcell region  
85 requires significant coordination and organization. Previously, we used dual-protein 2D-  
86 immunofluorescence microscopy (IFM) and high-resolution 3D-SIM to determine the  
87 relative localization patterns of pneumococcal division and PG synthesis proteins at  
88 different stages of division (10-12). Stages of cell division were assigned retrospectively  
89 based on static “snap-shot” images of cells from non-synchronized exponential cultures.  
90 These studies showed that in newly divided, predivisional (stage 1) daughter cells,  
91 division and PG synthesis proteins locate to an FtsZ-organized, midcell equatorial ring  
92 (Fig. S1). As nearly simultaneous sPG and pPG synthesis begin (stage 2) (17), the  
93 equatorial ring begins to constrict and becomes the new septal ring. Some FtsZ and  
94 associated proteins EzrA and FtsA move outward continuously with MapZ from the septal  
95 ring toward the positions of the future equatorial rings in daughter cells (13). As

96 constriction and midcell elongation continue, FtsZ amount decreases at the midcell of  
97 middle- to late-divisional cells and begins to accumulate at the equators of daughter cells.  
98 Meanwhile, PG synthesis proteins remain at the midcell septal ring.

99 At the resolution of standard 2D-epifluorescence microscopy (2D-EFM), essential  
100 class B bPBP2x transpeptidase (TP), which interacts with the FtsW SEDS  
101 glycosyltransferase (GT) to carry out sPG synthesis (13, 18), locates in an apparent inner  
102 ring within an outer ring containing the class B bPBP2b TP (11), which interacts with the  
103 RodA SEDS GT to carry out pPG synthesis (Fig. S1) (19, 20). Several other proteins  
104 implicated in pPG synthesis locate to this apparent outer ring, including MreC that  
105 organizes and may activate bPBP2b (21), class A aPBP1a that has both GT and TP  
106 activities (12), MltG endo-lytic transglycosylase that cleaves glycan chains (21), and StkP  
107 serine/threonine kinase that mediates cell division (11, 12). Near the end of cell division  
108 (stage 4), remaining PG synthesis proteins that have not moved to developing equatorial  
109 rings converge to a small spot between the daughter cells (Fig. S1) (11), before finally  
110 moving to the equatorial rings of the daughter cells (13).

111 Additional evidence for physical separation of the sPG and pPG synthesis machines  
112 midway through cell division was obtained by staining with fluorescent vancomycin (FL-  
113 Vanco), which labels PG pentapeptides in areas of PG synthesis (22), with fluorescent D-  
114 amino acids (FDAAs), which label PG in regions of active PBP TP activity (23, 24), and  
115 with an activity-based  $\beta$ -lactone fluorescent probe (7FL) specific for bPBP2x (25, 26). FL-  
116 Vanco labeling combined with IFM of mid-divisional cells indicated localization of bPBP2x  
117 inside of regions of nascent PG synthesis that were surrounded by bPBP2b and other  
118 pPG synthesis proteins (11). Long pulses of FDAAs for 5 min followed by 3D-SIM showed

119 labeling of a midcell ring surrounding a prominent central dot of FDAA labeling,  
120 resembling a “Saturn-like” pattern, in mid-divisional cells (11). Specific inhibition with the  
121  $\beta$ -lactam antibiotic methicillin and protein depletion experiments indicated that the central  
122 dot of septal TP activity is attributable to bPBP2x (11). Likewise, these central dots of  
123 FDAA labeling disappeared in rings of non-constricted septa in cells depleted for the  
124 GpsB regulatory protein (10). Last, spatial separation of bPBP2x was confirmed with a  
125 bPBP2x-specific, activity-based  $\beta$ -lactone fluorescent probe (7FL, Lac(L)-Phe-FL), whose  
126 labeling recapitulated a “Saturn-like” labeling pattern, indicating that although most active  
127 bPBP2x moves toward the center of the septum, some still remains in the outer peripheral  
128 ring (25, 26).

129 Limitations of these previous fluorescent-protein and -probe studies are the low  
130 resolution ( $\approx 250$  nm) of conventional 2D-EFM and of rotated 3D-SIM images (27). Due to  
131 their ovoid shape, *Spn* cells predominantly lie sideways along their long axis during  
132 imaging on a flat surface. Imaging of septal rings and associated structures in horizontal  
133 cells by 3D-SIM is limited by the Z-axial resolution of 250-300 nm of the system, which is  
134 much lower than the 100 nm resolution in the XY lateral plane (27). This axial resolution  
135 limitation remains when reconstructed image volumes of horizontally oriented cells are  
136 rotated by 90° to visualize septal rings as circles. To overcome this obstacle, we devised  
137 a simple method to reliably orient a small, but sufficient, number of *Spn* cells vertically  
138 onto their poles (i.e., “on their heads”) for 3D-SIM imaging, thereby enabling high lateral  
139 resolution of division rings. Using this approach, we were able to detect FDAA-labeled  
140 intermediate concentric rings of sPG synthesis TP activity in strains expressing  
141 fluorescent PG synthesis proteins. This approach located the proteins to the outer

142 peripheral or inner septal rings and showed that these proteins are organized as nodal  
143 structures distributed regularly around these rings in early divisional cells. We further  
144 found that short pulses of FDAA labeling also revealed nodal distributions of TP activity  
145 that were disrupted in division mutants. Together, these results reveal a highly uniform  
146 organization of coordinated PG synthesis and distinct separation of the sPG and pPG  
147 synthesis machines at the midcell of dividing ovococcal bacteria.

148

## 149 RESULTS

150 **“Snap-shots” of vertically oriented *Spn* cells labeled with FDAAs reveal**  
151 **constriction of concentric septal and peripheral rings.** To circumvent the lower  
152 resolution during rotation of 3D-SIM images, we devised a simple method to capture a  
153 sufficient number of vertically oriented, fixed *Spn* cells to image division planes at high  
154  $\approx 100$  nm  $\times$   $\approx 100$  nm XY lateral resolution. Wild-type (WT) D39  $\Delta cps$  cells were first  
155 labeled with a blue FDAA (HADA) for several generations and then with a red FDAA  
156 (TADA) for 2.5 min to label sites of new PG synthesis (Fig. 1A and 1B). Cells were fixed  
157 with formaldehyde and resuspended in a small amount of hardening anti-fade solution  
158 pipetted onto small, round glass coverslips onto which slides were placed. The anti-fade  
159 suspension medium minimized photobleaching, and its viscosity and the large number of  
160 cells in samples trapped some cells in a vertical orientation. This procedure led to a  
161 reliable, but small ( $\leq 1\%$ ), percentage of cells suspended on their poles, which could be  
162 spotted as circles (Fig. 1A and 1C), among many horizontally oriented cells (Fig. 1B) in  
163 each field.

164 Vertically oriented *Spn* cells were captured at different stages of the division cycle  
165 (Fig. 1A and 1C). In predivisional cells, red TADA labeling appears as a single ring around  
166 the division site (diagrammed in Fig. 1D). Remarkably, as division precedes, TADA  
167 labeling is detected in a pair of intermediate concentric rings, which are designated as the  
168 outer (peripheral) and inner (septal) rings. The inner ring represents the TP activity at the  
169 leading-edge of the closing septum annulus that eventually converges down to a dot,  
170 surrounded by the outer ring to form a “Saturn-like” pattern reported before, where the  
171 dot results from bPBP2x TP activity (11). In very late divisional cells, all remaining TADA  
172 labeling at midcell converges to a single dot at the division site, while new TADA rings  
173 appear at the equators of daughter cells. The regions of TP activity, including their  
174 relationship to membrane invagination, are summarized in Figure 1D. We conclude that  
175 PG synthesis occurs at two distinct, separate locations at the midcell of dividing *Spn* cells.

176 **bPBP2x and FtsZ primarily locate to the constricting inner septal ring, whereas**  
177 **bPBP2b and FtsX locate to the outer peripheral ring.** We reasoned that the spatial  
178 separation observed in vertically oriented *Spn* cells could be used to assign PG synthesis  
179 proteins to the sPG and/or pPG synthesis machine(s). We labeled strains expressing  
180 isfGFP-bPBP2x or sfGFP-bPBP2b with TADA (125  $\mu$ M) for a moderate time (2.5 min),  
181 and then observed TADA and GFP fluorescence in vertically oriented cells (Fig. 2 and  
182 S2). isfGFP-bPBP2x or sfGFP-bPBP2b was expressed from its native chromosomal  
183 locus, and cells expressing these constructs exhibited minimal discernible growth or cell  
184 morphology defects (Fig. S3A and S3B) (13). Western blotting with native antibody  
185 showed a single species of each fusion protein (Fig. S3C). Nevertheless, isfGFP-bPBP2x  
186 cellular amount is moderately increased (169%) compared to unlabeled WT bPBP2x,



187 whereas sfGFP-bPBP2b is underproduced to only 12-15% of the WT amount, without  
188 causing ostensible defects in cell growth and shape in BHI broth (Fig. S3). We  
189 characterized two other strains that express fusion constructs without causing defects in  
190 growth and morphology. In one strain, iHT-bPBP2x is expressed at  $\approx 164\%$  or  $\approx 88\%$  of  
191 WT bPBP2x level when grown in BHI broth or C+Y medium, respectively (Fig. S2C, S2E,  
192 and S3 A-C). In the second iHT-bPBP2b//P<sub>Zn</sub>-iHT-bPBP2b merodiploid strain grown in  
193 BHI broth containing 0.3 mM Zn<sup>2+</sup>/0.03 mM Mn<sup>2+</sup>, iHT-bPBP2b is expressed at  $\approx$ WT  
194 bPBP2b level ( $\approx 107\%$ ; Fig. S2D and S3C).

195 In predivisional cells grown in BHI broth, TADA treatment for 2.5 min labels equatorial  
196 rings fairly uniformly, whereas sfGFP-bPBP2x and sfGFP-bPBP2b appear as nodes  
197 distributed regularly around the circumference of cells (Fig. 2A and, S2A, row 1).  
198 Independent labeling of WT bPBP2x with the 7FL  $\beta$ -lactone probe specific for bPBP2x  
199 corroborated a nodal organization in predivisional equatorial rings of daughter cells (Fig.  
200 S2F). As division progresses, isfGFP-bPBP2x moves inward resulting in formation of the  
201 inner septal ring (Fig. 2A and S2A, row 2), with some bPBP2x remaining in the outer ring,  
202 as was also observed for labeling with the 7FL (Fig. S2F) (25, 26). Displacement between  
203 the single TADA ring and the inner isfGFP-bPBP2x ring (Fig. 2A and S2A, row 2) likely  
204 reflects the continued movement inward of isfGFP-bPBP2x during the time required to  
205 wash away unincorporated TADA and fix cells. As the TADA-labeled inner septal ring  
206 becomes more prominent, isfGFP-bPBP2x condenses into a dense, concentric ring  
207 largely lacking detectable nodes at this resolution, with some isfGFP-bPBP2x remaining  
208 in the outer ring (Fig. 2A and S2A, row 3).

209 A similar pattern of localization was observed for slightly overexpressed or  
210 underexpressed iHT-bPBP2x in cells grown in BHI broth or C+Y medium, respectively  
211 (Fig. S2C and S2E), including residual iHT-bPBP2x remaining in the outer ring. In iHT-  
212 protein fusion experiments, the blue FDAA HADA replaced TADA due to spectral overlap  
213 of the red HT-JF549 ligand with TADA. Nodes of iHT-bPBP2x (Fig. S2C and S2E) were  
214 often less distinct and regular than those of intrinsically fluorescent isfGFP-bPBP2x (Fig.  
215 2A and S2A), likely because of non-optimal labeling with the extrinsic HT substrate.

216 By contrast, as isfGFP-bPBP2x progresses to the inner septal ring during division (Fig.  
217 2A and S2A, row 3), sfGFP-bPBP2b expressed at a low level compared to WT bPBP2b  
218 remains confined to the outer peripheral ring, with little, if any sfGFP-bPBP2b detected in  
219 the inner ring marked by TADA (Fig. 2A and S2B, row 3). Likewise, iHT-bPBP2b  
220 expressed near the WT bPBP2b level remains as nodes in the outer peripheral ring of  
221 pre- and early divisional cells (Fig. S2D, row 1), but is not detected in the constricting  
222 inner septal ring (Fig. S2D, row 2). Again, extrinsically labeled iHT-bPBP2b nodes vary  
223 more than those of intrinsically fluorescent sfGFP-bPBP2b. Together, these results  
224 identify intermediate states of spatial separation of the bPBP2x-containing sPG and  
225 bPBP2b-containing pPG synthesis machines during *Spn* division (see Fig. 1D). The nodal  
226 localization of bPBP2x and bPBP2b in the midcell rings of predivisional cells is taken up  
227 below in the context of FDAA labeling patterns.

228 We extended this approach to a protein that had not been localized before. FtsX is a  
229 polytopic membrane protein that forms a complex with the cytoplasmic FtsE ATPase and  
230 the extracellular PcsB PG hydrolase in *Spn* (28-31). The FtsEX:PcsB complex is essential  
231 for *Spn* growth due to its role in hydrolytic remodeling during PG synthesis (28, 32, 33).

232 Depletion of FtsEX:PcsB results in the formation of chains of spheroid cells (31, 33),  
233 characteristic of defective pPG synthesis (11, 28). To test this idea, we localized an FtsX'-  
234 isfGFP-FtsX' sandwich fusion in vertically oriented *Spn* cells (Fig. S2G). This FtsX  
235 sandwich fusion is expressed from the normal chromosomal locus and does not cause  
236 cell defects, even though about 60% seemed to be proteolytically cleaved once in the  
237 extracellular ECL1 domain near the fusion point (Fig. S3C). Throughout the cell cycle,  
238 FtsX-isfGFP-FtsX' appears as nearly evenly spaced nodes around the outer peripheral  
239 ring demarked by TADA labeling and was not detected in the inner septal ring later in  
240 division (Fig. S2G). Finally, we determined that FtsZ-sfGFP tracks with TP activity at the  
241 leading-edge of the closing septum annulus (Fig. S2H). We conclude that PG remodeling  
242 by the FtsEX:PcsB complex is likely confined to pPG synthesis in *Spn*, and that FtsEX  
243 and pPG synthesis is not associated with an FtsZ ring during much of the *Spn* cell cycle  
244 (see Fig. 1D). In addition, this example illustrates the utility of using FDAA labeling as a  
245 fiducial marker to distinguish proteins involved in sPG and/or pPG synthesis.

246 **New PG synthesis is organized as a series of regularly spaced nodes around**  
247 **the midcell of predivisional *Spn* cells.** At a labeling time of 2.5 min with 125  $\mu$ M TADA,  
248 we observed apparent nodal variation of TADA intensity in the outer and inner rings of  
249 dividing *Spn* cells (Fig. 1 and 2). As noted above, we also observed nodal positioning of  
250 bPBP2x, bPBP2b, and FtsX in these rings (Fig. 2 and S2). To study these patterns further,  
251 we labeled WT *Spn* cells with a lower concentration of TADA (45  $\mu$ M) for a very short  
252 pulse (17 s) before imaging vertically oriented cells (Fig. 3). To maximize the spacing  
253 between nodes, we confined our analysis of TADA labeling patterns to predivisional cells  
254 that have the largest diameters by inspection and that were relatively plentiful in fields of

255 non-synchronized cultures. Very short pulses resolved TADA labeling into a series of  
256 regularly spaced nodes distributed around the equators of predivisional *Spn* cells (Fig.  
257 3A).

258 To quantify the pattern of these nodes, we developed a custom vertical image analysis  
259 graphical user interface (VIMA-GUI) using MATLAB (see *Experimental Procedures*). After  
260 manually designating individual nodes in each division ring, the program accurately  
261 determines the location of the ring, the diameter of the cell, the number of FDAA nodes,  
262 and the arc distance between adjacent nodes. TADA pulse-labeled and fixed WT  $\Delta cps$   
263 D39 cells have an average diameter of  $0.84 \mu\text{m} \pm 0.05$  (SD), indicating that the selected  
264 cells are at the same predivisional stage (Fig. 3A; Table S3). WT  $\Delta cps$  D39 cells contain  
265 an average of  $9.8 \pm 1.0$  (SD) individual TADA-labeled nodes, with an average arc distance  
266 between nodes of  $0.27 \mu\text{m} \pm 0.07$  (SD) (Fig. 3B; Table S3). The consistency of these  
267 measurements strongly supports the notion of an ordered placement of TP activity sites  
268 early in *Spn* division.

269 **The pattern of FDAA-labeled nodes is not caused by image processing.** To  
270 confirm that the regular nodal TADA-labeling pattern was not caused by the processing  
271 steps required for rendering structured illumination images, we examined the raw data  
272 and data-process parameters for TADA-pulse-labeled WT  $\Delta cps$  D39 cells (Fig. 1 and 3).  
273 Nodal labeling was still observed at the equators of pulse-labeled predivisional *Spn* cells  
274 using conventional, low-resolution ( $\approx 250$  nm) widefield 2D-EFM without image  
275 deconvolution (arrows, Fig. 4A). Deconvolution improved the clarity of the nodes in these  
276 low-resolution widefield images, but the images remained blurry compared to 3D-SIM  
277 images (Fig. 3A). To examine the influence of the major user-defined data smoothing

278 function in SIM reconstruction, we processed 3D-SIM data by adjusting the Wiener filter  
279 setting stepwise between 0.001-0.02 (34). Higher filter settings (above 0.01) resulted in  
280 clear “honeycomb” patterning effects on the sample and in background regions. We found  
281 no discernable patterning or grouping (e.g., over-separation of intensity into nodes) of  
282 signal with settings below 0.006 (Fig. 4B, row 2) and set the Wiener filter at 0.001 for the  
283 data presented in this work (Fig. 4B, row 1). Finally, we asked if the level of fluorescence  
284 signal in the pulse-labeled cells was potentially contributing to an artificial separation of  
285 signal into nodes. To this end, we determined the maximal pixel peak intensities in lines  
286 drawn through nodes in cells labeled for 17s (Fig. 3) and through the nearly contiguous  
287 labeling rings of cells labeled for 2.5 min (Fig. 1). Background offsets were determined  
288 from regions lacking cells for the two labeling conditions, and these backgrounds were  
289 subtracted from the mean maximal pixel intensities. The mean maximal pixel intensity of  
290 nodes (425 A. U.  $\pm$  105) was similar to that of nearly contiguous rings (461 A. U.  $\pm$  169),  
291 indicating that the SIM processing can produce nearly contiguous rings and separate  
292 nodes at about the same intensity level. This equivalence argues that the observed nodes  
293 are not simply being created by grouping together regions of low fluorescence signal. We  
294 conclude that the 3D-SIM processing parameters used in these analyses did not create  
295 the TADA nodal patterns observed in vertical *Spn* cells.

296 In support of this conclusion, the nodal pattern of TADA labeling becomes irregular in  
297 mutants defective in FtsZ ring assembly or in the regulation of PG synthesis (next  
298 section). This irregularity is not consistent with an image reconstruction artifact. In one  
299 experiment, FtsZ was expressed from a Zn<sup>2+</sup>-inducible promoter in a  $\Delta ftsZ//P_{Zn-ftsZ^+}$   
300 merodiploid strain grown in BHI broth containing sufficient Zn<sup>2+</sup> to allow growth

301 comparable to the WT strain. The merodiploid strain was shifted to BHI broth lacking  $Zn^{+2}$   
302 for 2.5 h, which resulted in enlarged spheroid cells with increased ( $\approx 1.4$ -fold) diameters  
303 (Fig. 5; Table S3). The FtsZ-depleted and WT FtsZ<sup>+</sup> strain were pulse-labeled (17 s) with  
304 TADA, and vertically oriented cells were imaged by 3D-SIM. WT cells show a regular  
305 nodal pattern in  $\approx 94\%$  of vertical cells, whereas the FtsZ-depleted cells with larger  
306 diameters show a regular nodal pattern in only  $\approx 40\%$  of cells (Fig. 5A). The remaining  
307  $\approx 60\%$  of FtsZ-depleted cells show irregular nodal arrangements, often with large gaps  
308 between nodes (arrow, Fig. 5A). “Regular” and “irregular” nodal patterns were initially  
309 distinguished by visual heuristic criteria, where “regular” refers to nodal patterns that  
310 appear by eye to be relatively evenly distributed, whereas “irregular” refers nodal  
311 distributions that contain one or more large gaps with spacing estimated to be at least  
312 twice that in the regular nodal pattern. Subsequent measurements of arc lengths  
313 generally matched the initial visual criteria. FtsZ-depleted cells with regular patterns  
314 contained more TADA-labeled nodes than WT or FtsZ-depleted cells with irregular  
315 patterns (Fig. 5B, middle; Table S3). The mean distance between nodes was greater for  
316 FtsZ-depleted than WT cells, with the variability of gap distances in FtsZ-depleted cells  
317 with irregular patterns reflected by a high standard deviation (Fig. 5B, right; Table S3).  
318 Taken together, this evidence strongly argues that the FDAA nodes are not an artifact of  
319 3D-SIM imaging and that FtsZ is required to maintain the WT arrangement of FDAA nodes  
320 in predivisional *Spn* cells.

321 **The number of regularly spaced FDAA-labeled nodes is correlated with the**  
322 **diameter of predivisional *Spn* cells.** The increase in the number of nodes in FtsZ-  
323 depleted cells with regular spacing (Fig. 5B, middle; Table S3) was suggestive of a

324 regulatory mechanism for node placement. To explore this idea, we determined labeling  
325 patterns in five additional division and PG synthesis mutants that were pulsed with TADA  
326 for 17 s and imaged vertically (Fig. 6). Amino acid changes in FtsZ(G107S) (divisome ring  
327 organizer protein) (13), EzrA(T506I) (FtsZ-ring modulator in Gram-positive bacteria) (35),  
328 and GpsB(K96N) (regulator of the balance between sPG and pPG synthesis) (10, 36)  
329 cause temperature sensitivity (TS) at 42°C. TS mutants expressing EzrA(T506I) or  
330 GpsB(K96N) were isolated for this study (Table S1). At the semi-permissive temperature  
331 of 37°C in BHI broth, each mutant grows slower and forms cells with enlarged diameters  
332 (Fig. S4A; Table S3). The TADA-labeling pattern of each mutant was similar to that of the  
333 FtsZ-depleted strain. The majority (53% to 66%) of mutant cells show irregular nodal  
334 patterns with gaps and greater arc distances, whereas cells with regular labeling patterns  
335 contain an increased number of nodes spaced similarly to WT (Fig. 6A, 6B, and S4B;  
336 Table S3).

337 We extended this analysis to  $\Delta pbp1a$  and  $\Delta khpA$  mutants that have significantly  
338 smaller diameters than WT cells in BHI broth (Fig. S4A, Table S3).  $\Delta pbp1a$  mutants lack  
339 aPBP1a and produce skinny, slightly elongated cells (21, 37), while  $\Delta khpA$  mutants lack  
340 a regulatory RNA-binding protein and form smaller cells with the same aspect ratio as  
341 larger WT cells (38). The nodal pattern in the  $\Delta pbp1a$  or  $\Delta khpA$  mutant is regular in >90%  
342 of cells with an average arc distance similar to that of WT (Fig 6A and 6B; Table S3);  
343 consequently, the mutant cells have fewer nodes per cell (Fig. S4B). When plotted, these  
344 data show that the number of regularly spaced nodes, when present, increases linearly  
345 with ring diameter (Fig. 6C), consistent with a mechanism that maintains WT spacing  
346 between sites of PG synthesis in predivisional *Spn* cells.

347           **Spacing of bPBP2x and bPBP2b nodes is similar to that of FDAA nodes**  
348 **produced by short pulse labeling.** The number and arc distance of nodes of isfGFP-  
349 bPBP2x and sfGFP-bPBP2b in the midcell rings of predivisional cells (Fig. 2A, S2A, S2B,  
350 and 7A) were measured and found to be similar to those of the FDAA nodes in WT cells  
351 (Fig. 2B and 7C; Table S3). Notably, the spacing of the TADA (red) and sfGFP-bPBP2b  
352 (green) nodes determined in the same cell is similar, but displaced in most cells (Fig. 7A),  
353 providing further support that the nodal patterns are not a microscopy artifact. To  
354 quantitate the relative distributions of these patterns, we calculated correlation  
355 coefficients for the number and spatial distribution of TADA and sfGFP-bPBP2b nodes in  
356 48 cells (Fig. S5A and S5B). As expected by the number of nodes (Table S3), there is a  
357 positive correlation between the number of sfGFP-bPBP2b and TADA nodes (Fig. S5A).  
358 In contrast, spatial correlation coefficients were distributed around 0, indicating no strong  
359 interdependence of the positions of the TADA and sfGFP-bPBP2b nodes (Fig. S5B).

360           We performed two additional labeling protocols to gain information about these  
361 patterns. First, we performed tandem short-pulse labeling of WT cells with TADA (17 s),  
362 which labels regions of active TP activity, followed by Boc-FL (21 s), which labels all active  
363 PBPs (Fig. 7B; Table S3). Displaced two-color patterns of TADA and Boc-FL nodes were  
364 produced, similar to those of TADA-labeled sfGFP-bPBP2b cells (Fig. 7A). Again, there  
365 was a positive correlation between the number of TADA and Boc-FL nodes (Fig. S5C),  
366 but no spatial correlation of the positions of the two kinds of nodes in 18 cells (Fig. S5D).  
367 The regular nodal pattern after Boc-FL pulse-labeling pattern did not match what would  
368 be expected from an earlier study done at long labeling times (39). We reprised this earlier  
369 study and obtained different results (*Appendix SI, Additional data*; Fig. S6), consistent



370 with those reported here (Fig. 7B). Last, we tandemly pulse labeled WT cells with three  
371 different colors of FDAAs (green, then red, then blue) (Fig. S7). We again observed  
372 regular, displaced nodal patterns for each color of FDAA probe (arrows, Fig. S7),  
373 supporting the conclusion that there is a distributive, regular nodal pattern of PBP  
374 localization and TP activity at the midcell ring of predivisional *Spn* cells.

### 375 **FDAA labeling is organized in nodes in other ovoid-shaped bacterial species.**

376 To determine if this regular, organized pattern of TP activity by PBPs is present in other  
377 ovococcal species, we labeled *Streptococcus mitis* and *Enterococcus faecalis* with short  
378 (17 s) pulses of TADA and imaged vertically oriented cells by 3D-SIM (Fig. 8). *S. mitis* is  
379 a close evolutionary relative that exchanges DNA with *Spn* by natural competence, while  
380 *E. faecalis* is more evolutionarily distant in the same *Lactobacillale* order (40-42). Both  
381 species demonstrated a pattern of TADA-labeled nodes at midcell with an average arc  
382 distance indistinguishable from that of WT *Spn* (Fig. 8B; Table S3). Thus, the regular  
383 organized pattern of PBP TP activity in predivisional cells is widely distributed in  
384 ovococcal species.

385

## 386 **DISCUSSION**

387 Whether the sPG and pPG synthesis machines of *Spn* are distributed contiguously in  
388 a single midcell ring (“plum pudding” model) or separate from each other during septal  
389 constriction has been a point of contention (11, 43-45). The demonstration of concentric  
390 intermediate rings of TP activity reported here provides strong support for the separation  
391 hypothesis (Fig. 1D and 9A). Localization of bPBP2x to the inner ring, which corresponds  
392 to the constricting leading edge of the septal annulus, further supports closure driven by

393 PG synthesis by the bPBP2x:FtsW complex (13, 18). Some bPBP2x remains in the outer  
394 ring of mid-to-late divisional cells when iHT-bPBP2x is expressed at near WT level in C+Y  
395 medium (Fig. S2E) or when WT bPBP2x is itself labeled with the 7FL probe (Fig. S2F)  
396 (25). Thus, active bPBP2x is both at the constricting leading edge of the septal annulus  
397 and at its outer edge, suggesting expansion of the annulus in both places. The constricting  
398 FtsZ ring also tracks with sPG synthesis at the leading edge of the septal annulus ring,  
399 implying that FtsZ is not detectable in the outer pPG synthesis ring (Fig. S2H).

400 In contrast, bPBP2b expressed at 12% or at WT levels primarily localizes to the outer  
401 pPG synthesis ring (Fig. 2A, S2B, S2D, and S3C). These results indicate that only about  
402 12% of bPBP2b cellular amount is sufficient for normal growth and *Spn* cell morphology  
403 (Fig. S3A and S3B), implying that bPBP2b is in excess in cells in this culture condition.  
404 An implication of confinement of bPBP2b to the outer midcell ring is that the presumed  
405 circumferential movement of the bPBP2b:RodA complex during pPG synthesis is guided  
406 by a structure that lacks FtsZ filaments/bundles. *Spn* does not encode the actin-like MreB  
407 protein that mediates PG elongation of rod-shaped bacteria (4), and determination of *Spn*  
408 elongasome composition and organization is an area of active research.

409 FtsX is also confined to the outer pPG synthesis ring (Fig. S2G). FtsX is an essential,  
410 polytopic membrane protein that forms a complex with the cytoplasmic FtsE ATPase and  
411 the extracellular PcsB PG hydrolase in *Spn* (28-32). Depletion of essential FtsX, FtsE, or  
412 PcsB results in chains of spherical cells, similar to those caused by depletion of bPBP2b  
413 (11, 28, 30, 31, 33, 46). An FtsX'-isfGFP-FtsX' fusion was detected in the outer PG  
414 synthesis ring, but not in the inner septal ring (Fig. S2G), consistent with a role for  
415 FtsEX:PcsB in pPG synthesis, analogous to that played by FtsEX:CwI/O in sidewall PG

416 synthesis in *Bacillus subtilis* (*Bsu*) (47, 48). Thus, *Spn* FtsX is in proximity to FtsZ and  
417 FtsA in the nascent divisome in early predivisional cells (Fig. S2G); however, in contrast  
418 to *E. coli* FtsX (49), as division proceeds, *Spn* FtsX physically separates from FtsZ and  
419 FtsA, which are at the leading edge of the septal annulus (Fig. S2H). This result raises  
420 the possibility that a PG remodeling hydrolase other than FtsEX:PcsB mediates sPG  
421 synthesis. Based on these examples, dual labeling of vertical cells can be applied to  
422 assign other PG synthesis, divisome, and regulatory proteins to the sPG or pPG synthesis  
423 machines of *Spn*. This approach may also explicate PG stress responses, such as  
424 possible roles of Class A PBPs in imparting resistance to an exogenously added PG  
425 hydrolase following exposure of *Spn* laboratory strain R6 to a  $\beta$ -lactam antibiotic that  
426 inhibits bPBP2x (and DacA (PBP3)) (14).

427 We noted that bPBP2x and bPBP2b are distributed in regular nodal patterns at the  
428 equators of predivisional cells (Fig. 2, 7A, and S2 A-F). As the inner ring constricts, this  
429 nodal pattern becomes more compact and difficult to resolve (Fig. 2A); hence, we  
430 confined this study to the large equators of predivisional cells (Fig. 3A). By shortening the  
431 FDAA pulse time down from 2.5 min to  $\approx 17$  s, we observed that TP activity also is  
432 distributed in a regular nodal pattern with  $\approx 10$  nodes separated by an average arc length  
433 of  $0.27 \pm 0.07$   $\mu\text{m}$  in WT cells (Fig. 3B). A comparable nodal pattern of FDAA pulse  
434 labeling was detected in *S. mitis* and *E. faecalis* (Fig. 8), indicating a common organization  
435 of TP activity in predivisional ovococcal cells.

436 Several controls support the conclusion that the nodal pattern was not caused by  
437 processing steps required to generate structured illumination images (see *Results*). Most  
438 importantly, the regular nodal pattern of FDAA labeling was disrupted by gaps in a

439 majority of cells depleted for FtsZ (Fig. 5) or in temperature-sensitive *ftsZ*(G107S),  
440 *ezrA*(T506I), and *gpsB*(K96N) mutants grown at the semi-permissive temperature of 37°C  
441 (Fig. 6). Each of these growing TS mutants formed enlarged cells with increased  
442 diameters compared to WT (Fig. S4). Between 34%-47% of these larger mutant cells still  
443 showed regular nodal patterns of FDAA labeling with more nodes per ring spaced at the  
444 WT arc distance (Fig. 6). Conversely,  $\Delta$ *pbp1a* or  $\Delta$ *khpA* mutants have smaller diameters  
445 than WT with fewer FDAA nodes spaced at the WT arc distance (Fig. 6). Together, these  
446 data are consistent with a mechanism that maintains a regular spacing of PG synthesis  
447 in predivisional cells, irrespective of equator diameter (Fig. 6C and 9B).

448 The average arc distance was similar between nodes of FDAA labeling, isfGFP-  
449 bPBP2x, isfGFP-bPBP2b, and Boc-FL (Fig. 2, 3, and 7). However, the positioning of  
450 nodes in two-color FDAA/sfGFP-bPBP2b or FDAA/Boc-FL experiments showed low  
451 correlation (Fig. S5), as did nodes sequentially pulse-labeled with three different colors of  
452 FDAAs (Fig. S7). The displacement of FDAA nodes relative to bPBP2b or Boc-FL, may  
453 reflect the time ( $\approx$ 1 min) that it takes to wash away unincorporated FDAA. It is also  
454 possible that PBPs other than bPBP2b are active in predivisional cells. Altogether, these  
455 results indicate that the placement of PBPs and TP activity is not fixed at single positions  
456 on equators of predivisional cells, but rather, is dynamic and distributive.

457 The localization of PG synthesis and PBPs in early divisional cells varies among  
458 bacterial species that use different modes of septum formation and division. Similar to the  
459 patterns reported here for *Spn* and other ovococcal species (Fig. 2, 8, and S2), labeling  
460 *Eco* for short pulses, but not for long times, with an FDAA results in nodal (also called  
461 punctate) patterns, which were not quantitated at high resolution (50). Consistent with

462 nodal pattern formation, high-resolution microscopy of vertically oriented *Eco* cells  
463 revealed a pattern of “discrete densities” of mCit-FtsI (bPBP3) distributed around the  
464 entire septal ring of dividing *Eco* cells (51).

465 Different FDAA pulse-labeling patterns were reported for *S. aureus* (*Sau*) and *Bsu*  
466 compared to those in *Spn* and *Eco*. Discrete foci of PG synthesis were not observed in  
467 *Sau* cells labeled with short FDAA pulses and viewed by 3D-SIM, in an experiment similar  
468 to Figure 3, or labeled with a pulse of other D-amino acid probes and viewed by  
469 localization microscopy (52). However, while not commented upon, SIM images of sfGFP-  
470 PBP1 in some vertically oriented *Sau* cells do appear nodal around closing septal rings  
471 (53), and heterogenous localization of *Sau* GFP-PBP2 has also been reported (54).  
472 Labeling *Bsu* with short, sequential pulses of two colors of FDAAs or an FDAA followed  
473 by Boc-FL (55) gave a different pattern from the regular nodal pattern in *Spn* (Fig. 7 and  
474 S7). At the lower resolution of rotated 3D-SIM images, sequential labeling with two colors  
475 of FDAAs gives a pattern suggestive of a limited number of PG synthesis complexes  
476 moving in both directions around the septum. Labeling *Bsu* with an FDAA followed by  
477 Boc-FL again suggests a surprisingly limited number of active PBP complexes labeled by  
478 Boc-FL adjacent to newly synthesized PG marked by the FDAA (55). We conclude that  
479 nodal PG synthesis at septa occurs in different patterns in some bacteria and is  
480 apparently absent in others, possibly reflecting different mechanisms of sPG synthesis  
481 and cell separation. In this regard, *Spn* and *Eco* simultaneously close division septa while  
482 separating daughter cells (13, 50), whereas septa formation by PG synthesis occurs  
483 before cell separation in *Sau* and *Bsu* (52, 53, 55).

484 The mechanism that causes the regular nodal distribution of PBPs and their TP activity  
485 in predivisional cells of *Spn* remains to be determined (Fig. 9B). Recent notable studies  
486 have demonstrated heterogeneous supramolecular localization of membrane proteins  
487 generally and at septa of *Sau* cells, including interacting enzymes that catalyze  
488 phospholipid biosynthesis and the MreD regulator of PG synthesis (56, 57). This  
489 heterogeneous localization results in punctate patterns of these proteins at division septa,  
490 resembling the localization of *Spn* PBPs reported here (Fig. 2 and S2). Polytopic MreD  
491 plays a role in supramolecular localization of the phospholipid biosynthesis enzymes, and  
492 heterogeneous punctate patterns are lost upon protein overexpression (57). A favored  
493 explanation for punctate supramolecular organization is that membrane protein  
494 complexes distort local curvature on membranes and thereby perturb diffusion, resulting  
495 in distribution patterns for the majority of membrane proteins (57). Whether membrane  
496 protein distribution, the size and composition of PG synthesis complexes, an unknown  
497 scaffolding complex, or a combination of these mechanisms causes the nodal distribution  
498 of PBPs and TP activity in predivisional *Spn* cells remains to be determined.

499 Finally, single molecules of bPBP2x and its interacting partner FtsW move  
500 circumferentially around the septa of dividing pneumococcal cells in either direction at  
501  $\approx 21 \pm 8$  (SD) nm/s (13). Based on data in that paper, runs extend for  $\approx 28 \pm 15$  (SD) s ( $n$   
502 = 106 cells). In contrast, bPBP2x and FtsW not bound to septa move diffusively  
503 throughout the cell membrane (13, 58). In *Spn*, movement of the bPBP2x:FtsW complex  
504 at septa is driven by PG synthesis itself and not by treadmilling movement of FtsZ  
505 filaments/bundles (13). In the static images here, we do not precisely know how many  
506 molecules form the bPBP and FDAA-labeled nodes; but, a reasonable assumption is that

507 each node consists of multiple PBPs and regions of PG labeling. With this in mind,  
508 circumferentially moving bPBP2x:FtsW complexes likely move linearly in both directions  
509 across nodal regions driven by the PG synthesis echoed by FDAA labeling. Aggregate  
510 movements of these heterogenous nodal complexes with time would then account for the  
511 distributive, non-correlated labeling patterns in two-color pulse labeling experiments (Fig.  
512 7B and S7). This and other hypotheses about the composition, organization, and dynamic  
513 movement of these nodal PG synthesis complexes in *Spn* and other ovococcal bacteria  
514 await future testing.

515

## 516 **EXPERIMENTAL PROCEDURES**

517 Detailed experimental procedures are described in *SI Appendix, Experimental*  
518 *Procedures*, including bacterial strains (Tables S1 and S2) and growth conditions; growth  
519 curve analysis; 2D-epifluorescence and phase-contrast microscopy of *Spn* cells;  
520 saturating labeling with Boc-FL and Ceph-CT; FDAAs used; quantitative western blotting  
521 of relative cellular amounts of WT and fusion proteins; localization in vertical *Spn* cells of  
522 the following probes after the indicated labeling times: HADA ( $\approx$ 100 min) then TADA (2.5  
523 min), TADA (2.5 min) in cells expressing isfGFP-bPBP2x, sfGFP-bPBP2b, or FtsX'-  
524 isfGFP-FtsX', HADA (2.5 min) in cells expressing iHT-bPBP2x or iHT-bPBP2b, TADA (17  
525 s); localization of bPBP2x with 7FL in WT *Spn* and a  $\Delta$ *pbp1b* mutant; localization in  
526 vertical *Spn* cells of the following probes after the indicated labeling times: TADA (17 s),  
527 TADA (17 s) followed by Boc-FL (7 s), and BADA (40 s) followed by TADA (40 s) followed  
528 by HADA (40 s); image acquisition by 3D-SIM; analysis of FDAA node distributions using

529 a custom MATLAB GUI; widefield fluorescence microscopy; and bPBP2x and bPBP2b  
530 protein purification and antibody production.

531

## 532 **ACKNOWLEDGEMENTS**

533 We thank laboratory members and Erkin Kuru (Harvard Med Sch), Yves Brun  
534 (Université de Montréal), Seamus Holden (Newcastle Univ), and Jie Xiao (Johns Hopkins)  
535 for discussions and suggestions; Jim Powers (IUB) for help with microscopy, Luke Lavis  
536 (Janelia Lab) for Fluor JF549; Dalia Denapaite (Trento Univ), Reinhold Brückner, and  
537 Regine Hakenbeck (Kaiserlautern Univ) for anti-bPBP2x antibody; and Suzanne Walker  
538 and David Z. Rudner (Harvard Med Sch) for supporting preparation of anti-bPBP2x and  
539 anti-bPBP2b antibodies. This work was supported by NIH Grants RO1GM113172 (to  
540 M.S.V. and M.E.W.); RO1GM128439 (to E.E.C. and M.E.W.); R35GM131767 (to  
541 M.E.W.); R35GM136365 (to M.S.V), RO1AI148752 (to S. Walker), RO1AI139083 (To D.  
542 Z. Rudner), National Science Foundation Grant MCB1615907 (to S.L.S.); NIH  
543 Predoctoral Quantitative and Chemical Biology Training Grant T32 GM109825 (to A.J.P.);  
544 NIH Predoctoral Grant F31AI138430 (to M.M.L.); and NIH Equipment Grant  
545 S10OD024988 to the Indiana University Bloomington (IUB) Light Microscopy Imaging  
546 Center.

547

## 548 **REFERENCES**

- 549 1. A. J. Loughran, C. J. Orihuela, E. I. Tuomanen, *Streptococcus pneumoniae*: invasion  
550 and inflammation. *Microbiol Spectr* **7**, 10.1128/microbiolspec.GPP3-0004-2018  
551 (2019).
- 552 2. J. N. Weiser, D. M. Ferreira, J. C. Paton, *Streptococcus pneumoniae*: transmission,  
553 colonization and invasion. *Nat Rev Microbiol* **16**, 355-367 (2018).



- 554 3. A. Zapun, T. Vernet, M. G. Pinho, The different shapes of cocci. *FEMS Microbiol Rev*  
555 **32**, 345-360 (2008).
- 556 4. W. Vollmer, O. Massidda, A. Tomasz, The cell wall of *Streptococcus pneumoniae*.  
557 *Microbiol Spectr* **7**, 10.1128/microbiolspec.GPP3-0018-2018 (2019).
- 558 5. A. J. F. Egan, J. Errington, W. Vollmer, Regulation of peptidoglycan synthesis and  
559 remodelling. *Nat Rev Microbiol* **18**, 446-460 (2020).
- 560 6. A. J. Egan, J. Biboy, I. van't Veer, E. Breukink, W. Vollmer, Activities and regulation  
561 of peptidoglycan synthases. *Phil Trans Royal Soc London. Series B, Biolog Sci*  
562 **370**, 10.1098/rstb.2015.0031 (2015).
- 563 7. S. J. Siegel, J. N. Weiser, Mechanisms of Bacterial Colonization of the respiratory  
564 tract. *Ann Rev Microbiol* **69**, 425-444 (2015).
- 565 8. J. L. Rodriguez, A. B. Dalia, J. N. Weiser, Increased chain length promotes  
566 pneumococcal adherence and colonization. *Infect Immun* **80**, 3454-3459 (2012).
- 567 9. K. H. Berg, D. Straume, L. S. Havarstein, The function of the transmembrane and  
568 cytoplasmic domains of pneumococcal penicillin-binding proteins 2x and 2b  
569 extends beyond that of simple anchoring devices. *Microbiol*  
570 10.1099/mic.0.078535-0 (2014).
- 571 10. B. E. Rued *et al.*, Suppression and synthetic-lethal genetic relationships of  $\Delta$ *gpsB*  
572 mutations indicate that GpsB mediates protein phosphorylation and penicillin-  
573 binding protein interactions in *Streptococcus pneumoniae* D39. *Molec Microbiol*  
574 **103**, 931-957 (2017).
- 575 11. H. C. Tsui *et al.*, Pbp2x localizes separately from Pbp2b and other peptidoglycan  
576 synthesis proteins during later stages of cell division of *Streptococcus pneumoniae*  
577 D39. *Molec Microbiol* **94**, 21-40 (2014).
- 578 12. A. D. Land *et al.*, Requirement of essential Pbp2x and GpsB for septal ring closure in  
579 *Streptococcus pneumoniae* D39. *Molec Microbiol* **90**, 939-955 (2013).
- 580 13. A. J. Perez *et al.*, Movement dynamics of divisome proteins and PBP2x:FtsW in cells  
581 of *Streptococcus pneumoniae*. *Proc Nat Acad Sci USA* **116**, 3211-3220 (2019).
- 582 14. D. Straume *et al.*, Class A PBPs have a distinct and unique role in the construction of  
583 the pneumococcal cell wall. *Proc Nat Acad Sci USA* **117**, 6129-6138 (2020).
- 584 15. M. Aaron *et al.*, The tubulin homologue FtsZ contributes to cell elongation by guiding  
585 cell wall precursor synthesis in *Caulobacter crescentus*. *Molec Microbiol* **64**, 938-  
586 952 (2007).

- 587 16. L. P. Potluri, S. Kannan, K. D. Young, ZipA is required for FtsZ-dependent preseptal  
588 peptidoglycan synthesis prior to invagination during cell division. *J Bacteriol* **194**,  
589 5334-5342 (2012).
- 590 17. R. Wheeler, S. Mesnage, I. G. Boneca, J. K. Hobbs, S. J. Foster, Super-resolution  
591 microscopy reveals cell wall dynamics and peptidoglycan architecture in ovococcal  
592 bacteria. *Molec Microbiol* **82**, 1096-1109 (2011).
- 593 18. A. Taguchi *et al.*, FtsW is a peptidoglycan polymerase that is functional only in  
594 complex with its cognate penicillin-binding protein. *Nat Microbiol* **4**, 587-594  
595 (2019).
- 596 19. A. J. Meeske *et al.*, SEDS proteins are a widespread family of bacterial cell wall  
597 polymerases. *Nature* **537**, 634-638 (2016).
- 598 20. M. Sjodt *et al.*, Structural coordination of polymerization and crosslinking by a SEDS-  
599 bPBP peptidoglycan synthase complex. *Nat Microbiol* **5**, 813-820 (2020).
- 600 21. H. C. Tsui *et al.*, Suppression of a deletion mutation in the gene encoding essential  
601 PBP2b reveals a new lytic transglycosylase involved in peripheral peptidoglycan  
602 synthesis in *Streptococcus pneumoniae* D39. *Molec Microbiol* **100**, 1039-1065  
603 (2016).
- 604 22. R. A. Daniel, J. Errington, Control of cell morphogenesis in bacteria: two distinct ways  
605 to make a rod-shaped cell. *Cell* **113**, 767-776 (2003).
- 606 23. Y. P. Hsu *et al.*, Full color palette of fluorescent d-amino acids for in situ labeling of  
607 bacterial cell walls. *Chem Sci* **8**, 6313-6321 (2017).
- 608 24. E. Kuru *et al.*, In Situ probing of newly synthesized peptidoglycan in live bacteria with  
609 fluorescent D-amino acids. *Angew Chem Int Ed Engl* **51**, 12519-12523 (2012).
- 610 25. S. Sharifzadeh *et al.*, Novel electrophilic scaffold for imaging of essential penicillin-  
611 binding proteins in *Streptococcus pneumoniae*. *ACS Chem Biol* **12**, 2849-2857  
612 (2017).
- 613 26. S. Sharifzadeh *et al.*, Chemical tools for selective activity profiling of bacterial  
614 penicillin-binding proteins. *Meth Enzymol* **638**, 27-55 (2020).
- 615 27. S. Holden, Probing the mechanistic principles of bacterial cell division with super-  
616 resolution microscopy. *Curr Opin Microbiol* **43**, 84-91 (2018).
- 617 28. M. Alcorlo, D. Straume, J. Lutkenhaus, L. S. Havarstein, J. A. Hermoso, Structural  
618 characterization of the essential cell division protein FtsE and its interaction with  
619 FtsX in *Streptococcus pneumoniae*. *mBio*, **11**, 10.1128/mBio.01488-20 (2020).

- 620 29. B. E. Rued *et al.*, Structure of the large extracellular loop of Ftsx and its interaction  
621 with the essential peptidoglycan hydrolase Pcsb in *Streptococcus pneumoniae*.  
622 *mBio*, **10** 10.1128/mBio.02622-18 (2019).
- 623 30. L. T. Sham, S. M. Barendt, K. E. Kopecky, M. E. Winkler, Essential PcsB putative  
624 peptidoglycan hydrolase interacts with the essential FtsX<sup>Spn</sup> cell division protein in  
625 *Streptococcus pneumoniae* D39. *Proc Nat Acad Sci USA*, **108**, E1061-1069  
626 (2011).
- 627 31. L. T. Sham, K. R. Jensen, K. E. Bruce, M. E. Winkler, Involvement of FtsE ATPase  
628 and FtsX extracellular loops 1 and 2 in FtsEX-PcsB complex function in cell  
629 division of *Streptococcus pneumoniae* D39. *mBio* **4**, 10.1128/mBio.00431-13  
630 (2013).
- 631 32. S. G. Bartual *et al.*, Structural basis of PcsB-mediated cell separation in *Streptococcus*  
632 *pneumoniae*. *Nature Comm* **5**, 3842 (2014).
- 633 33. W. L. Ng, K. M. Kazmierczak, M. E. Winkler, Defective cell wall synthesis in  
634 *Streptococcus pneumoniae* R6 depleted for the essential PcsB putative murein  
635 hydrolase or the VicR (YycF) response regulator. *Molec Microbiol* **53**, 1161-1175  
636 (2004).
- 637 34. G. Komis *et al.*, Superresolution live imaging of plant cells using structured illumination  
638 microscopy. *Nature Prot* **10**, 1248-1263 (2015).
- 639 35. A. D. Land, Q. Luo, P. A. Levin, Functional domain analysis of the cell division inhibitor  
640 EzrA. *PloS One* **9**, 10.1371/journal.pone.0102616 (2014).
- 641 36. R. M. Cleverley *et al.*, The cell cycle regulator GpsB functions as cytosolic adaptor for  
642 multiple cell wall enzymes. *Nature Comm* **10**, 10.1038/s41467-018-08056-2  
643 (2019).
- 644 37. A. D. Land, M. E. Winkler, The requirement for pneumococcal MreC and MreD is  
645 relieved by inactivation of the gene encoding PBP1a. *J Bacteriol* **193**, 4166-4179  
646 (2011).
- 647 38. J. J. Zheng, A. J. Perez, H. T. Tsui, O. Massidda, M. E. Winkler, Absence of the KhpA  
648 and KhpB (JAG/EloR) RNA-binding proteins suppresses the requirement for  
649 PBP2b by overproduction of FtsA in *Streptococcus pneumoniae* D39. *Molec*  
650 *Microbiol* **106**, 793-814 (2017).
- 651 39. O. Kocaoglu *et al.*, Selective penicillin-binding protein imaging probes reveal  
652 substructure in bacterial cell division. *ACS Chem Biol* **7**, 1746-1753 (2012).
- 653 40. X. Y. Gao, X. Y. Zhi, H. W. Li, H. P. Klenk, W. J. Li, Comparative genomics of the  
654 bacterial genus *Streptococcus* illuminates evolutionary implications of species  
655 groups. *PloS One* **9**, 10.1371/journal.pone.0101229 (2014).

- 656 41. W. Ludwig *et al.*, The phylogenetic position of *Streptococcus* and *Enterococcus*. *J*  
657 *Gen Microbiol* **131**, 543-551 (1985).
- 658 42. O. Massidda, L. Novakova, W. Vollmer, From models to pathogens: how much have  
659 we learned about *Streptococcus pneumoniae* cell division? *Environ Microbiol* **15**,  
660 3133-3157 (2013).
- 661 43. A. Fleurie *et al.*, Interplay of the serine/threonine-kinase StkP and the paralogs DivIVA  
662 and GpsB in pneumococcal cell elongation and division. *PLoS Genet* **10**,  
663 10.1371/journal.pgen.1004275 (2014).
- 664 44. D. Straume, G. A. Stamsas, K. H. Berg, Z. Salehian, L. S. Havarstein, Identification  
665 of pneumococcal proteins that are functionally linked to penicillin-binding protein  
666 2b (PBP2b). *Molec Microbiol* 10.1111/mmi.13543 (2016).
- 667 45. B. David *et al.*, PBP2b plays a key role in both peripheral growth and septum  
668 positioning in *Lactococcus lactis*. *PloS One* **13**, 10.1371/journal.pone.0198014  
669 (2018).
- 670 46. K. H. Berg, G. A. Stamsas, D. Straume, L. S. Havarstein, Effects of low PBP2b levels  
671 on cell morphology and peptidoglycan composition in *Streptococcus pneumoniae*  
672 R6. *J Bacteriol* **195**, 4342-4354 (2013).
- 673 47. Y. R. Brunet, X. Wang, D. Z. Rudner, SweC and SweD are essential co-factors of the  
674 FtsEX-CwlO cell wall hydrolase complex in *Bacillus subtilis*. *PLoS Genet* **15**,  
675 10.1371/journal.pgen.1008296 (2019).
- 676 48. J. Meisner *et al.*, FtsEX is required for CwlO peptidoglycan hydrolase activity during  
677 cell wall elongation in *Bacillus subtilis*. *Molec Microbiol* **89**, 1069-1083 (2013).
- 678 49. S. Pichoff, S. Du, J. Lutkenhaus, Roles of FtsEX in cell division. *Res Microbiol* **170**,  
679 374-380 (2019).
- 680 50. X. Yang *et al.*, GTPase activity-coupled treadmilling of the bacterial tubulin FtsZ  
681 organizes septal cell wall synthesis. *Science* **355**, 744-747 (2017).
- 682 51. B. Söderström, H. Chan, D. O. Daley, Super-resolution images of peptidoglycan  
683 remodelling enzymes at the division site of *Escherichia coli*. *Curr Genet* **65**, 99-  
684 101 (2019).
- 685 52. V. A. Lund *et al.*, Molecular coordination of *Staphylococcus aureus* cell division. *eLife*  
686 **7**, 10.7554/eLife.32057 (2018).
- 687 53. J. M. Monteiro *et al.*, Peptidoglycan synthesis drives an FtsZ-treadmilling-independent  
688 step of cytokinesis. *Nature* **554**, 528-532 (2018).

- 689 54. M. P. Strauss *et al.*, 3D-SIM super resolution microscopy reveals a bead-like  
690 arrangement for FtsZ and the division machinery: implications for triggering  
691 cytokinesis. *PLoS Biol* **10**, 10.1371/journal.pbio.1001389 (2012).
- 692 55. A. W. Bisson-Filho *et al.*, Treadmilling by FtsZ filaments drives peptidoglycan  
693 synthesis and bacterial cell division. *Science* **355**, 739-743 (2017).
- 694 56. J. Garcia-Lara *et al.*, Supramolecular structure in the membrane of *Staphylococcus*  
695 *aureus*. *Proc Nat Acad Sci USA* **112**, 15725-15730 (2015).
- 696 57. F. Weihs *et al.*, Heterogeneous localisation of membrane proteins in *Staphylococcus*  
697 *aureus*. *Sci Reports* **8**, 10.1038/s41598-018-21750-x (2018).
- 698 58. J. W. McCausland *et al.*, Treadmilling FtsZ polymers drive the directional movement  
699 of sPG-synthesis enzymes via a Brownian ratchet mechanism. *BioRxiv*  
700 10.1101/857813 (2020).

701

## 702 **FIGURE LEGENDS**

703 **Fig. 1.** 3D-SIM of vertically oriented *Spn* cells labeled with FDAAs reveals spatially  
704 distinct, concentric midcell ring intermediates of TP activity at different stages of division.  
705 (A) Schematic of labeling procedure (*top*). WT cells (IU1945) were labeled with 125  $\mu$ M  
706 HADA for several generations (old cell wall; cyan), washed, and labeled with 125  $\mu$ M  
707 TADA for 2.5 min (new cell wall from  $\approx$ 7% of a generation; red). Cells were fixed and  
708 prepared for vertical cell imaging by 3D-SIM (see *SI Appendix, Experimental Procedures*).  
709 Representative images are shown of rings from pre-, early, and late-division stages  
710 estimated by the diameters of outer TADA rings. Left images, HADA and TADA channels  
711 overlaid; right images TADA channel only. (B) Representative horizontally oriented cells  
712 from the same field as (A) locating the concentric rings at constricting midcell regions. (C)  
713 Montage of manually sorted *Spn* cells in different stages of cell division. Only the TADA  
714 is shown, and images are representative of >50 cells from more than three independent  
715 biological replicates. (D) Diagrammatic summary based on data in *Results* of the

716 organization of sPG and pPG synthesis in *Spn*, including concentric rings of new PG  
717 synthesis, membrane invagination, and proteins located in this study. Curved arrows  
718 indicate the image rotations indicated.

719 **Fig. 2.** bPBP2x or bPBP2b locate to the leading edge of the septal ring annulus or to  
720 the outer peripheral ring, respectively, at midcell in vertically oriented *Spn* cells. Cells  
721 expressing isfGFP-bPBP2x (IU11157) or sfGFP-bPBP2b (IU9965) were labeled with 125  
722  $\mu$ M TADA for 2.5 min, fixed, and prepared for vertical cell imaging by 3D-SIM (see *SI*  
723 *Appendix, Experimental Procedures*). (A) Representative images of cells (6 to 29) at  
724 different stages of division. isfGFP-bPBP2x and sfGFP-bPBP2b, pseudo-colored cyan;  
725 TADA labeling, pseudo-colored red. Brightness and contrast were manually adjusted to  
726 show signals associated with division rings and to reduce background lacking TADA  
727 labeling. Progression of cell division was indicated by the separation of the inner (septal)  
728 and outer (peripheral) rings. Cellular amounts of fluorescent-proteins produced relative to  
729 untagged WT protein in a control strain (see Fig. S3C) are in parentheses. (B)  
730 Quantitation of nodal distributions of isfGFP-bPBP2x and sfGFP-bPBP2b (but not TADA)  
731 in predivisional *Spn* cells with single, overlapping rings of TADA and GFP labeling.  
732 Distributions of ring diameters (left), nodes per ring (middle), and arc distances (right)  
733 were determined as described in *SI Appendix, Experimental Procedures*. Graphs show  
734 median (interquartile range; whiskers, 5<sup>th</sup>-95<sup>th</sup> percentile; +, mean). Means  $\pm$  SD from two  
735 independent biological replicates are shown below the graphs and compiled in Table S3.  
736 Differences between means were compared by a two-tailed *t* test (GraphPad Prism). \*,  
737  $P < 0.05$  and \*\*\*,  $P < 0.001$ .

738 **Fig. 3.** PBP TP activity is organized into regular nodes at the midcell of predivisional  
739 *Spn* cells. WT cells (IU1945) were incubated for 17 s with a low concentration of TADA  
740 (45.5  $\mu$ M), fixed, and prepared for vertical cell imaging by 3D-SIM (see *SI Appendix,*  
741 *Experimental Procedures*). (A) Representative images of 12 predivisional *Spn* cells  
742 pulsed-labeled with TADA. Mean ring diameter  $\pm$  SD of >60 cells from >3 independent  
743 biological replicates was determined as described in *SI Appendix, Experimental*  
744 *Procedures*. (B) Distributions of arc distances (*top*) and number of nodes per ring (*bottom*)  
745 determined for the data set of cells in (A) and compiled in Table S3.

746 **Fig. 4.** TADA-labeled nodes at the midcell of vertically oriented predivisional *Spn* cells  
747 are observed by widefield microscopy and at different 3D-SIM filter settings. WT cells  
748 (IU1945) were labeled with 45.5  $\mu$ M TADA for 17 s, fixed, and prepared for vertical cell  
749 imaging as described in *SI Appendix, Experimental Procedures*. (A) Representative  
750 widefield-microscopy images of four separate cells, before and after deconvolution.  
751 Arrows point to nodes of TADA labeling. (B) 3D-SIM images processed with different  
752 Wiener filter settings of the midcell of a single TADA-labeled vertical cell (top row) or a  
753 background region lacking a cell (bottom row). Red box, 0.001 Wiener filter setting used  
754 throughout this paper for 3D-SIM imaging. Scale bar = 1  $\mu$ m.

755 **Fig. 5.** FtsZ-depleted cells have enlarged midcell diameters, and a majority of cells  
756 have irregularly spaced nodes of TP activity. IU8124 ( $\Delta$ *ftsZ*//*P*<sub>Zn</sub>-*ftsZ*<sup>+</sup>) cells were grown  
757 in BHI broth containing 0.2 mM ZnCl<sub>2</sub> to ectopically express FtsZ for 12 h prior to  
758 depletion. IU8124 cells were diluted into BHI broth without added ZnCl<sub>2</sub> and incubated to  
759 deplete FtsZ (see *SI Appendix, Experimental Procedures*). After 2.5 h, WT (IU1945) and  
760 FtsZ-depleted cells were labeled with 45.5  $\mu$ M TADA for 17 s, fixed, and prepared for

761 vertical cell imaging by 3D-SIM (*SI Appendix, Experimental Procedures*). (A)  
762 Representative 3D-SIM images of nodes of TP activity in midcell rings of predivisional  
763 cells. Labeling was classified as regular (Reg) or irregular (Irreg) with gaps of varying  
764 sizes between nodes (white arrow) as described in *Results*. Percentages refer to analysis  
765 of 76 WT and 47 FtsZ-depleted cells. (B) Distributions of midcell ring diameters (left),  
766 nodes per ring (middle), and arc distances (right) of WT and FtsZ-depleted cells were  
767 determined as described in *SI Appendix, Experimental Procedures*. Ring diameters and  
768 nodes per ring were determined for 76 WT cells and for 19 or 28 Reg or Irreg FtsZ-  
769 depleted cells, respectively. Arc distance were determined for 746 nodes in WT cells and  
770 for 230 or 293 nodes in Reg or Irreg FtsZ-depleted cells, respectively. Graphs show  
771 median (interquartile range; whiskers, 5<sup>th</sup>-95<sup>th</sup> percentile; +, mean). Means  $\pm$  SD are  
772 compiled in Table S3. Differences in means relative to WT were determined by one-way  
773 ANOVA with Bonferonni's multiple comparison posttest (GraphPad Prism). \*\*\*,  $P < 0.001$ .

774 **Fig. 6.** Arc distance between regularly spaced midcell TP nodes is constant in  
775 predivisional *Spn* mutants with decreased or increased diameters compared to WT.  
776 Mutant strains of *S. pneumoniae* with altered midcell diameters were labeled with 45.5  
777  $\mu$ M TADA for 17 s, fixed, and prepared for vertical cell imaging by 3D-SIM as described  
778 in *SI Appendix, Experimental Procedures*. Strains used were:  $\Delta$ *pbp1a* (K164),  $\Delta$ *khpA*  
779 (E751), WT (IU1945), *ftsZ*(G107S) (IU10612), *ezrA*(T506I) (IU11034), and *gpsB*(K96N)  
780 (IU11956) (Table S1). (A) Representative 3D-SIM images of TP activity in midcell rings  
781 of predivisional cells. Percentages indicate the frequency of regularly spaced nodes (Reg)  
782 or irregularly spaced nodes (Irreg) with gaps (see white arrows) for the number of cells  
783 analyzed of each strain. Irregularly spaced nodes were observed in the majority of



784 *ftsZ*(G107S), *ezrA*(T506I) and *gpsB*(K96N) cells, whose diameters were greater than that  
785 of WT (see Fig. S4 and Table S3). (B) Distributions of arc distances between TP nodes  
786 of WT and mutant strains were determined as described in *SI Appendix, Experimental*  
787 *Procedures*. Graphs show median (interquartile range; whiskers, 5<sup>th</sup>-95<sup>th</sup> percentile; +,  
788 mean). Means  $\pm$  SD are compiled in Table S3. Cells with irregular midcell nodal patterns  
789 exhibit large SDs. Differences in means relative to WT were determined by one-way  
790 ANOVA with Bonferonni's multiple comparison posttest (GraphPad Prism). \*\*\*,  $P < 0.001$ .  
791 (C) Linear relationship between ring diameter (X-axis) versus nodes per ring (Y-axis) for  
792 WT and mutant strains with regular nodal patterns. Colored crosses represent  
793 measurements from single rings determined as described in *SI Appendix, Experimental*  
794 *Procedures* and shown in Fig. S4. Line of best fit and  $r^2$  values for the combined data set  
795 were determined using GraphPad Prism.

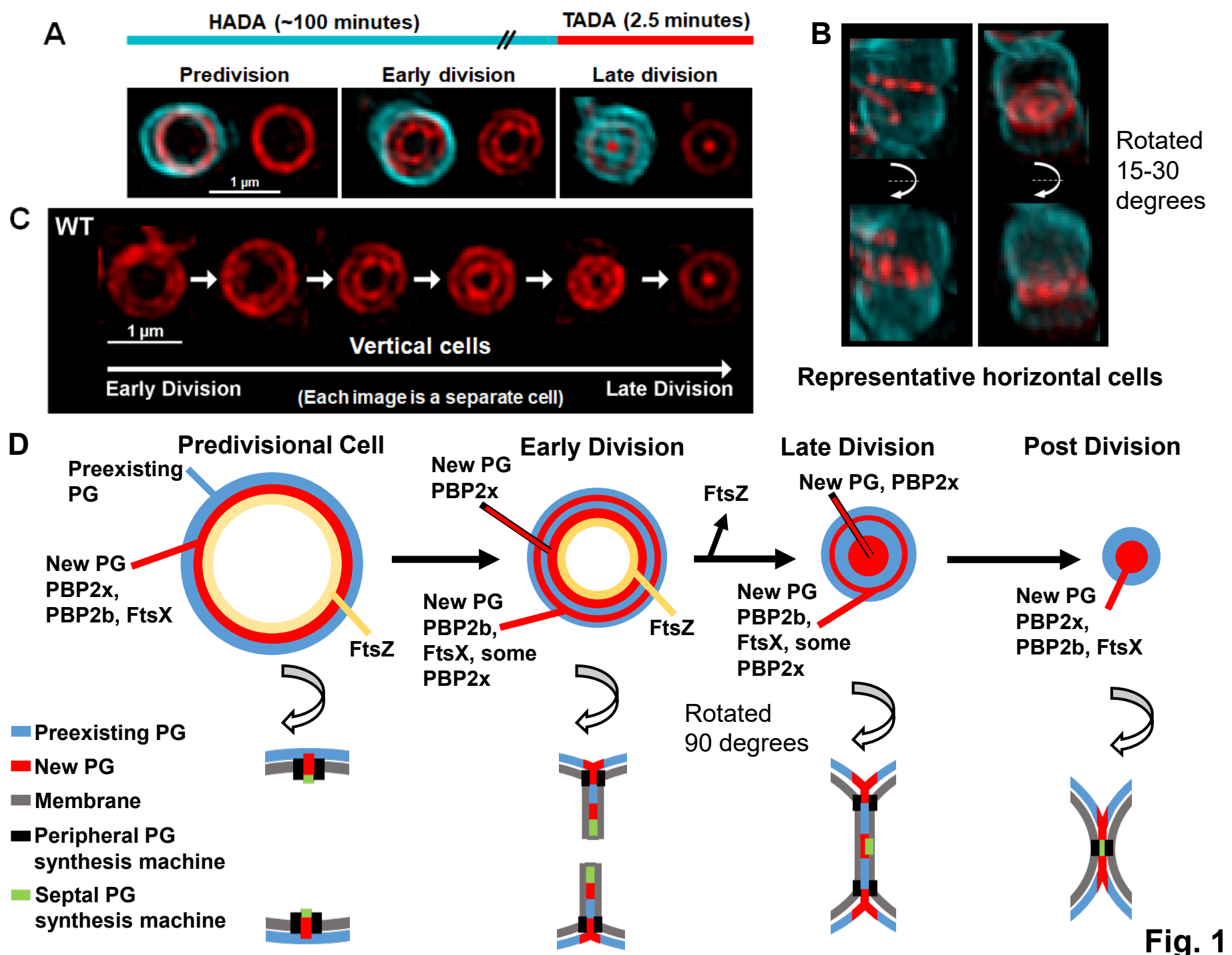
796 **Fig. 7.** sfGFP-bPBP2b and Bocillin-FL (Boc-FL) labeling are organized in nodal  
797 patterns at the midcell of predivisional *Spn* cells. Cells expressing sfGFP-bPBP2b  
798 (IU9965) were labeled with 45.5  $\mu$ M of TADA for 17 s, fixed, and prepared for vertical cell  
799 imaging by 3D-SIM as described in *SI Appendix, Experimental Procedures*. WT (IU1945)  
800 cells were pulse-labeled with TADA for 17 s, followed by labeling with 2  $\mu$ g/mL of Boc-FL  
801 for 21 s, fixed, and prepared for imaging (see *SI, Appendix, Experimental Procedures*).  
802 (A) Representative images of IU9965 localizing sfGFP-bPBP2b and TADA as nodes.  
803 Each row is a separate cell. (B) Representative images of WT cells localizing Boc-FL and  
804 TADA as nodes. Each row is a separate cell. (C) Distributions of ring diameters (left),  
805 nodes per ring (middle), and arc distances (right) for WT cells labeled with TADA alone,  
806 IU9965 (sfGFP-bPBP2b) labeled with TADA, IU9965 (sfGFP-bPBP2b) not labeled with

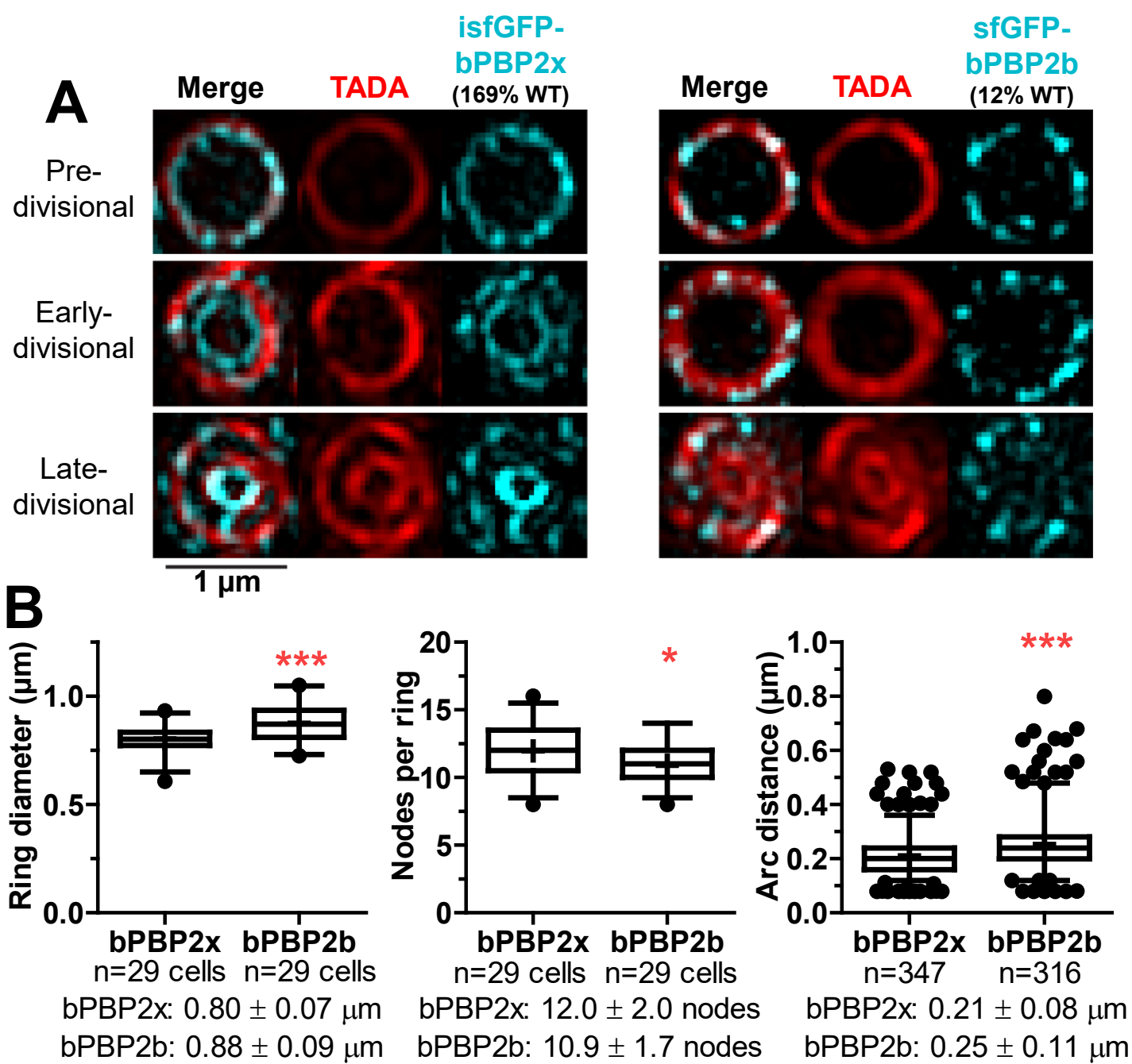
807 TADA, WT labeled with TADA followed by Boc-FL, and WT labeled with Boc-FL alone.  
808 Measurements were performed as described in *SI Appendix, Experimental Procedures*.  
809 Graphs show median (interquartile range; whiskers, 5<sup>th</sup>-95<sup>th</sup> percentile; +, mean). Means  
810  $\pm$  SD are compiled in Table S3. Differences in means relative to WT labeled with TADA  
811 were determined by one-way ANOVA with Bonferonni's multiple comparison posttest  
812 (GraphPad Prism). \*,  $P < 0.05$ ; \*\*\*,  $P < 0.001$ . Correlation coefficient analyses are presented  
813 in Fig. S5 and *Results*.

814 **Fig. 8.** The nodal pattern of regularly spaced TP activity at the midcell of predivisional  
815 cells is conserved in other ovoid-shaped bacterial species. *S. pneumoniae* (*Spn*, IU1945),  
816 *S. mitis* (*Smi*, ATCC 49456) and *E. faecalis* (*Efa*, ATCC 51299) cells were labeled with  
817 45.5  $\mu$ M TADA for 17 s, fixed, and prepared for vertical cell imaging by 3D-SIM (see *SI*  
818 *Appendix, Experimental Procedures*). (A) Representative images of two predivisional  
819 cells pulse-labeled with TADA are shown for *Spn* (left), *S. mitis* (middle), and *E. faecalis*  
820 (right) from the total number of cells analyzed (bottom). (B) Distributions of ring diameters  
821 (left), nodes per ring (middle), and arc distances of ovoid-shaped cells. Measurements  
822 were performed as described in *SI Appendix, Experimental Procedures*. Graphs show  
823 median (interquartile range; whiskers, 5<sup>th</sup>-95<sup>th</sup> percentile; +, mean). Means  $\pm$  SD are  
824 compiled in Table S3. Differences in means relative to *Spn* were determined by one-way  
825 ANOVA with Bonferonni's multiple comparison posttest (GraphPad Prism). \*\*,  $P < 0.01$  and  
826 \*\*\*,  $P < 0.001$ .

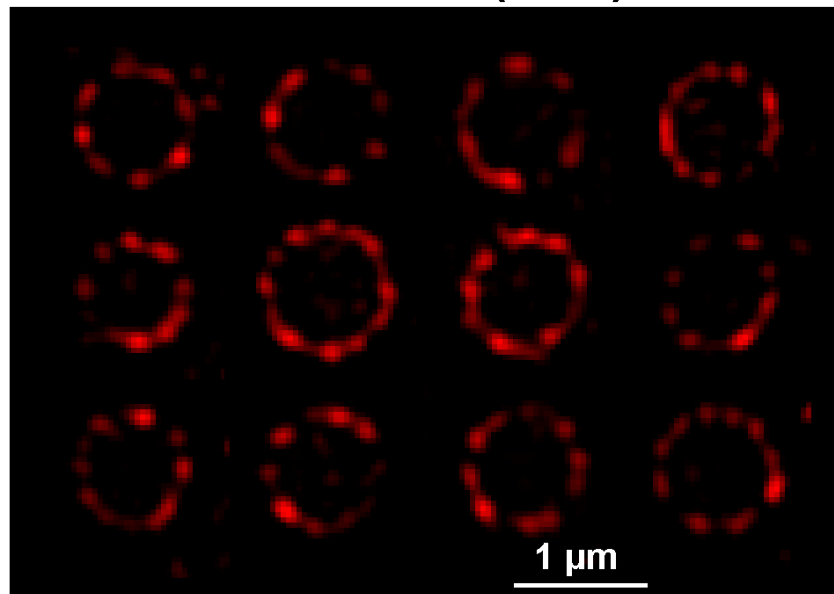
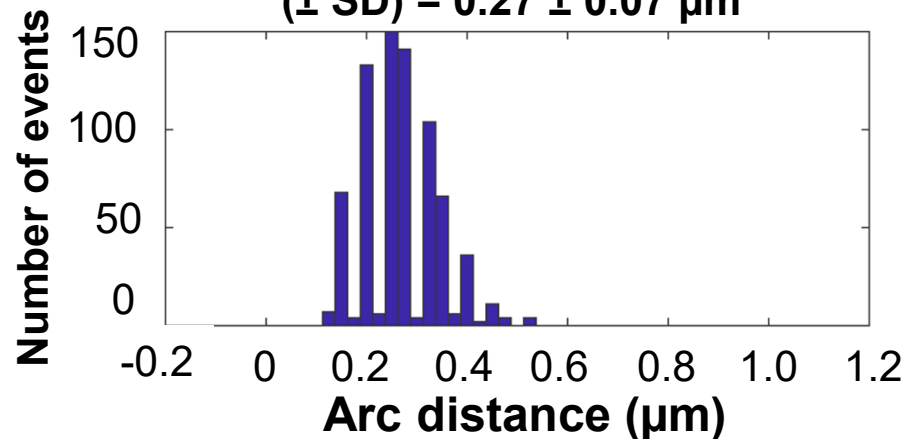
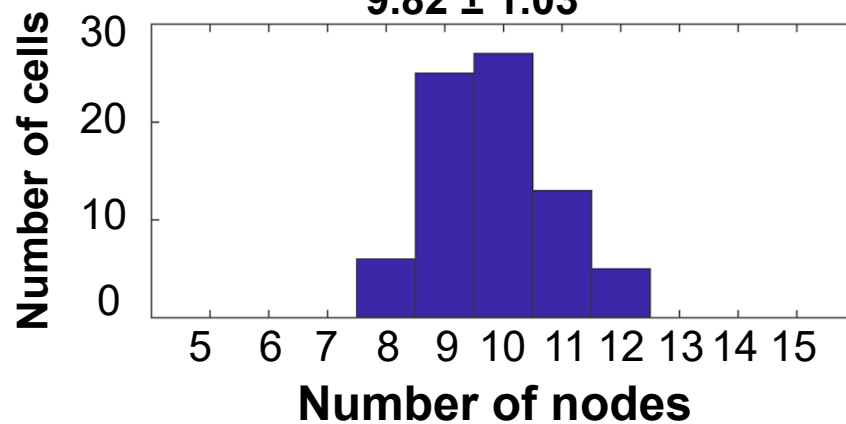
827 **Fig. 9.** Summary diagram of the localization PG synthesis in *Spn* based on results in  
828 this paper. (A) Separation of sPG and pPG (elongasome) machines at the midcell of  
829 dividing *Spn* cells. Cell division begins at the midcell equator of newly divided

830 predivisional cells in FtsZ-organized divisome rings containing the components of the  
831 sPG and pPG synthesis machines. Early in cell division the septal annulus forms and  
832 begins to close. The leading edge of the closing septal annulus separates the sPG  
833 machine from the pPG synthesis machine that remains at the outer edge of the annulus  
834 and elongates the PG outward from the midcell. The sPG machine contains bPBP2x TP,  
835 its partner FtsW GT, and other components, while the pPG synthesis machine is made  
836 up of bPBP2b TP and its partner RodA GT, other “Rod” complex proteins, and the  
837 FtsEX:PcsB remodeling PG hydrolase. The constricting FtsZ ring tracks with the leading  
838 edge of the septal annulus, such that the outer peripheral ring is not organized by FtsZ  
839 beyond the predivisional stage. Later in division, FtsZ remaining at the septum migrates  
840 to the developing equatorial rings in daughter cells. The inner sPG synthesis machine  
841 constricts into a dot surrounded by the closing outer pPG synthesis ring, which eventually  
842 constricts and merges with the sPG dot as the new cell pole is completed and the PG  
843 synthesis enzymes migrate to the new equatorial rings in daughter cells (see Fig. 1D  
844 also). (B) In predivisional cells, TP activity, sPG synthesis complexes, and pPG  
845 complexes are organized into a pattern of regularly spaced nodes (red circles). The  
846 placement of PBPs and TP activity is not fixed at single positions on equators of early  
847 divisional cells, but rather, is dynamic and distributive, likely driven by PG synthesis itself  
848 (13). Aggregate movements of these heterogeneous nodal complexes with time would  
849 account for the distributive, non-correlated nodal patterns observed in two-color labeling  
850 experiments. A constant distance ( $\approx 0.27 \mu\text{m}$ ) is maintained between nodes of PBP TP  
851 activity and between the PBPs themselves. Midcell rings of predivisional cells with smaller  
852 or larger diameters contain fewer or more nodes, respectively, than WT ( $\approx 10$  nodes).





**Fig. 2**

**A****WT TADA (17 s)**Mean ring diameter ( $\pm$ SD) =  $0.84 \pm 0.05 \mu\text{m}$ **B**Mean arc distance between nodes  
( $\pm$  SD) =  $0.27 \pm 0.07 \mu\text{m}$ Mean nodes per ring ( $\pm$  SD) =  
 $9.82 \pm 1.03$ **Fig. 3**

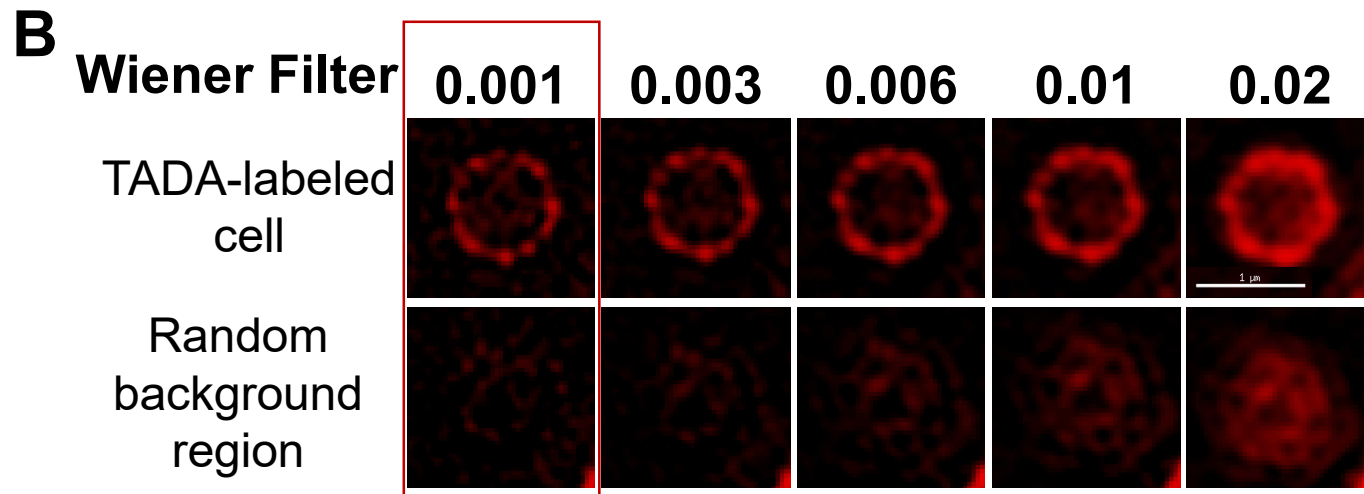
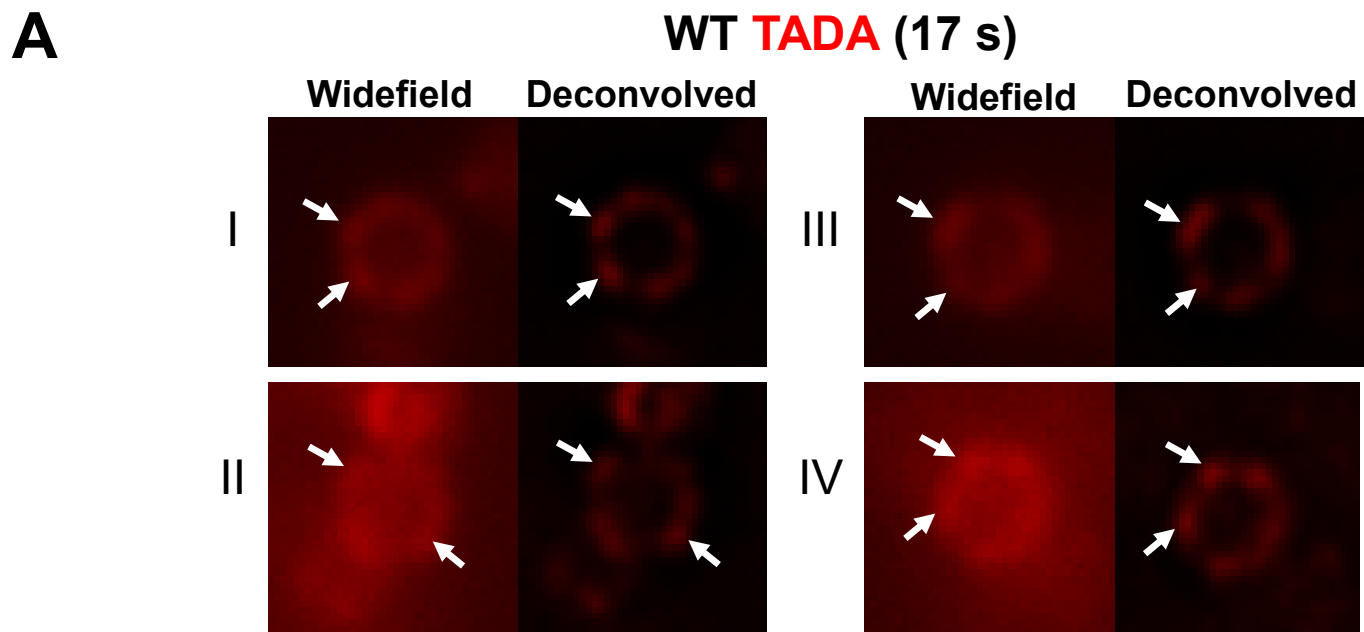


**Fig. 4**

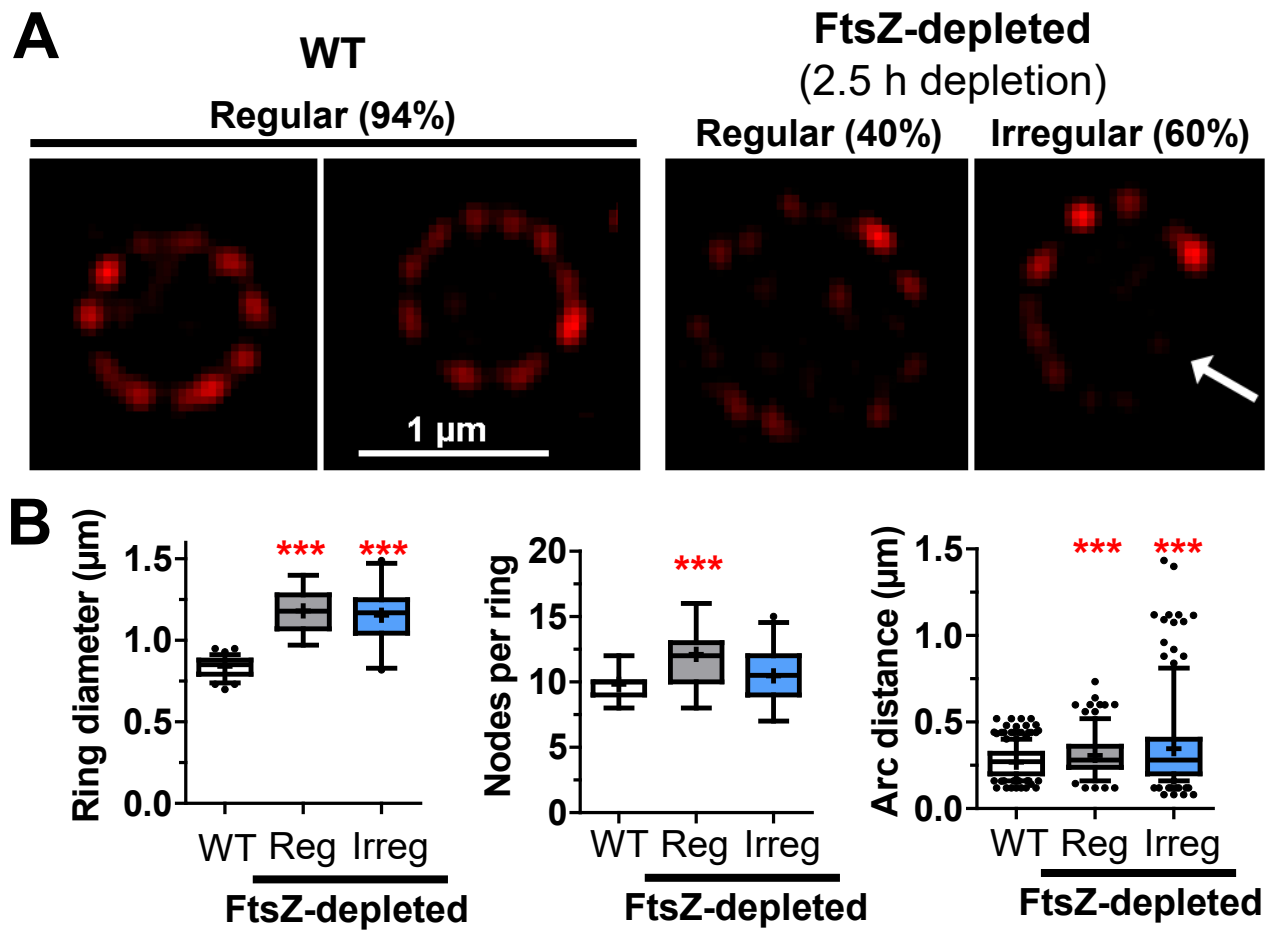


**Fig. 5**



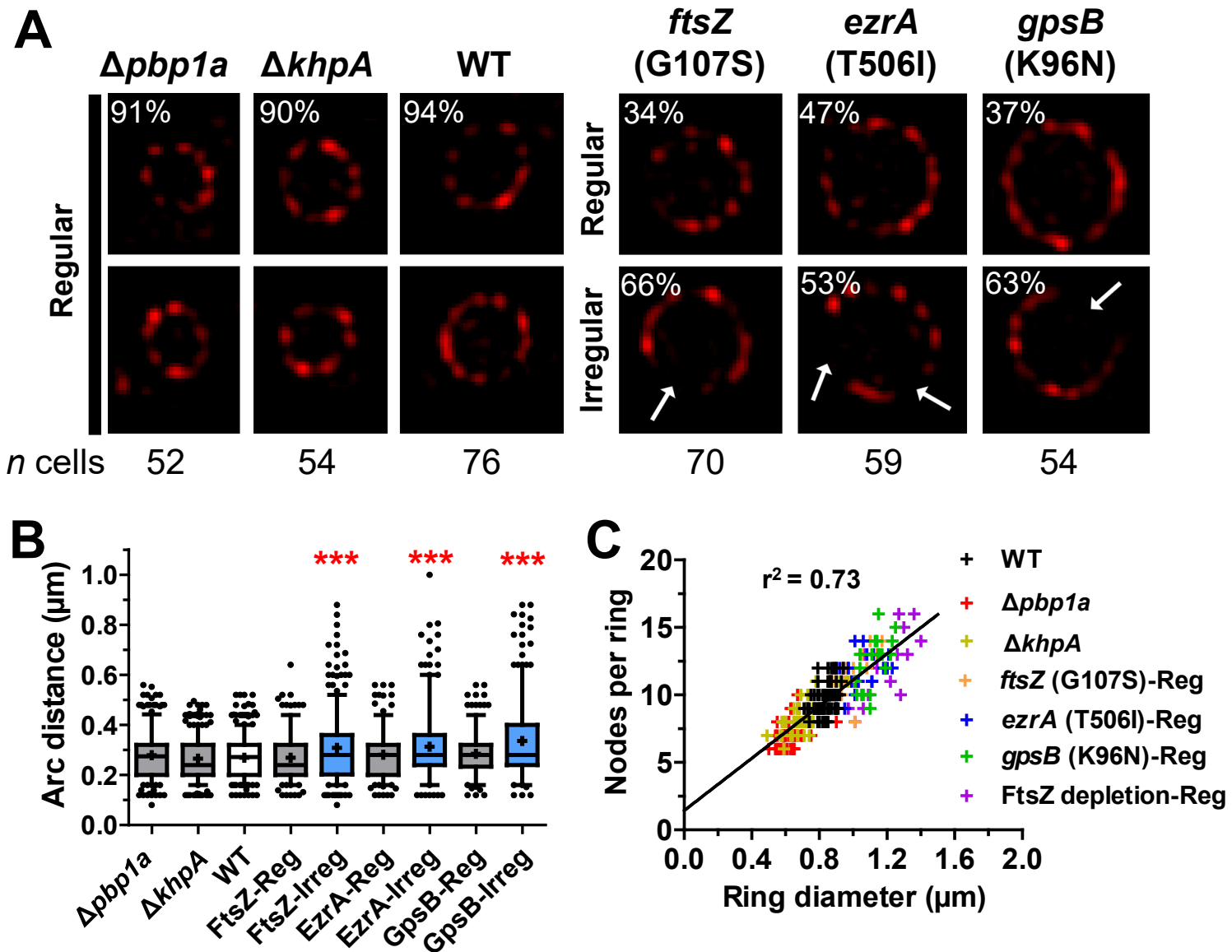


Fig. 6

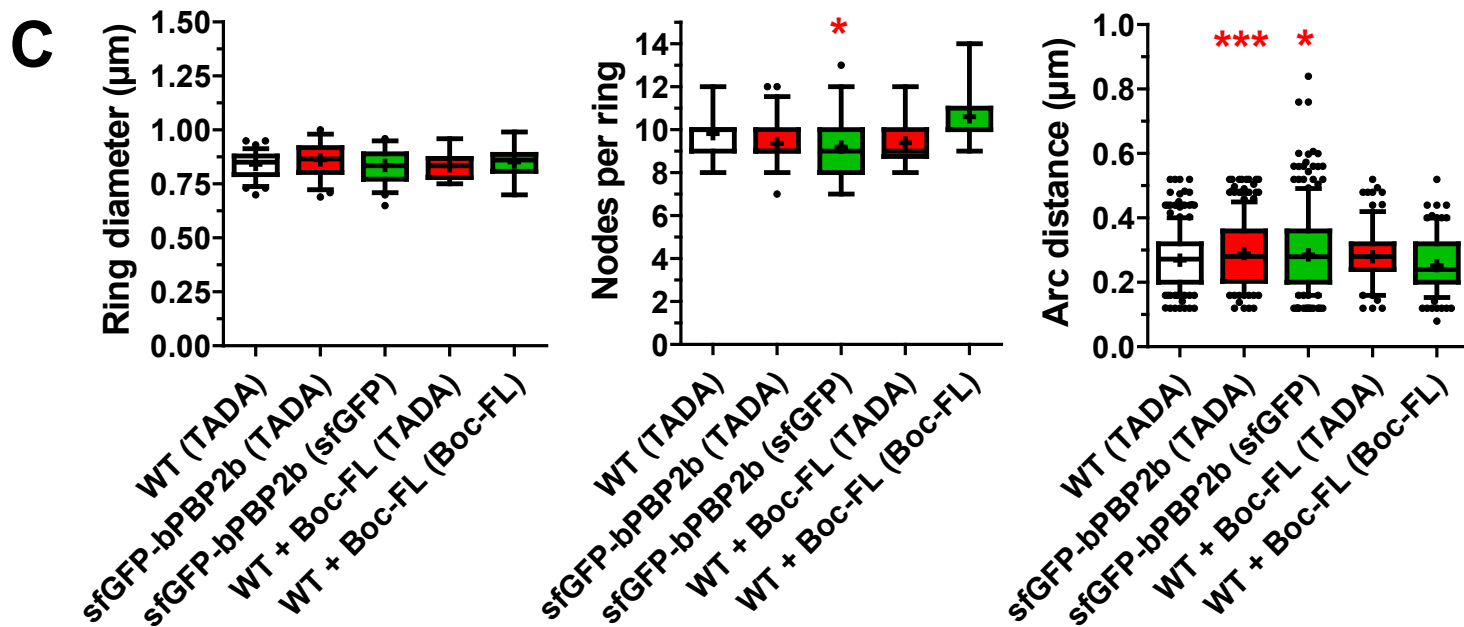
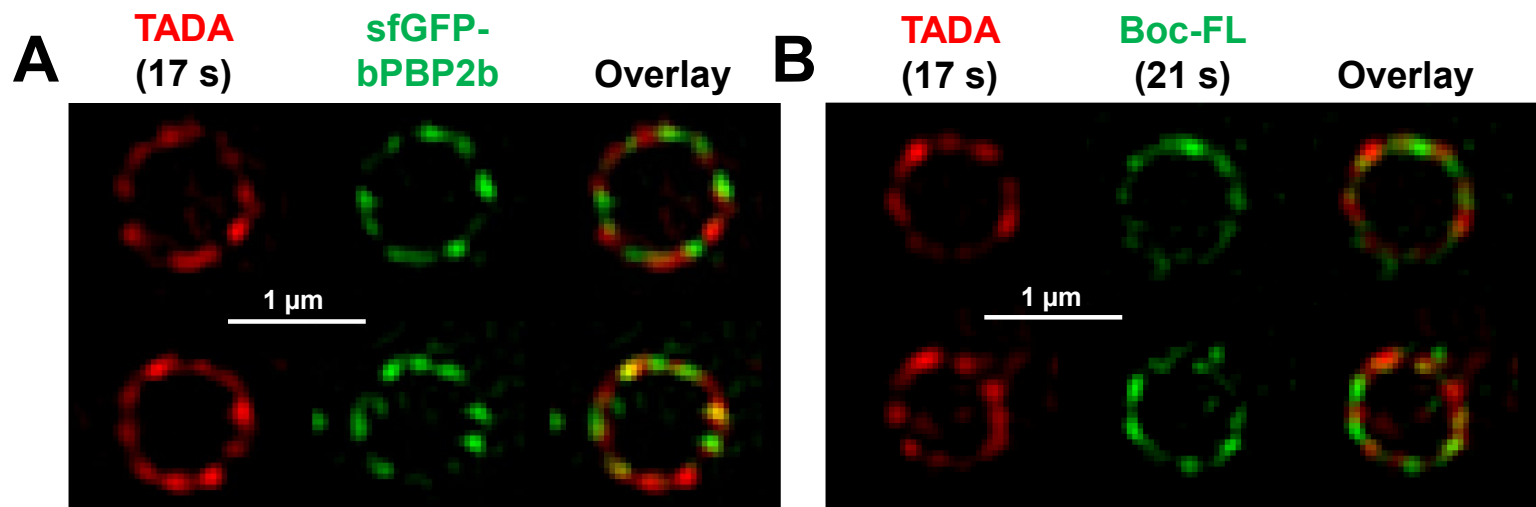
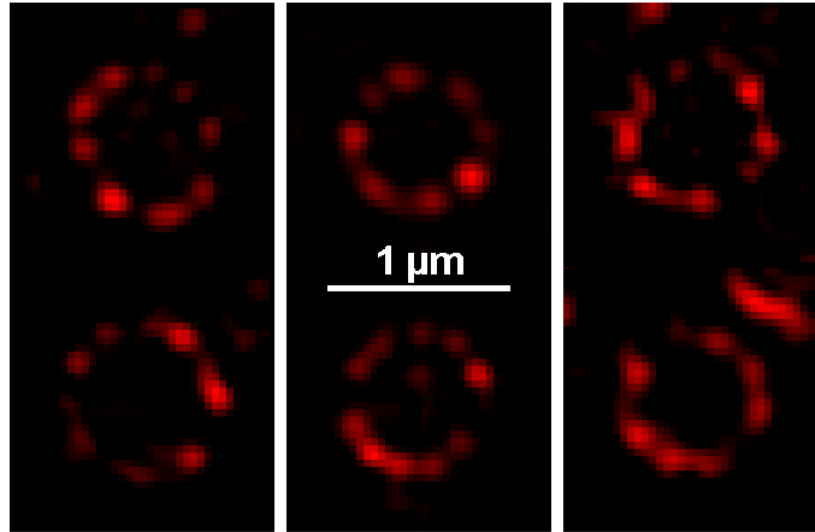


Fig. 7

**A** *S. pneumoniae*    *S. mitis*    *E. faecalis*



$n$  (cells) = 76

19

20

**B**

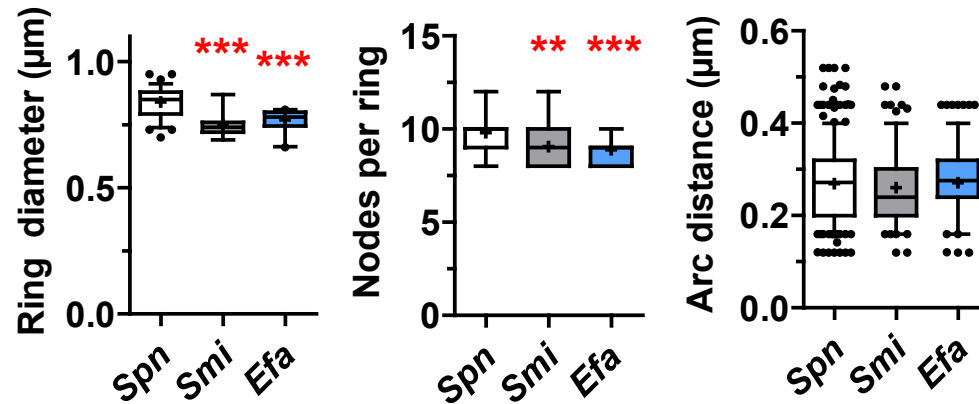
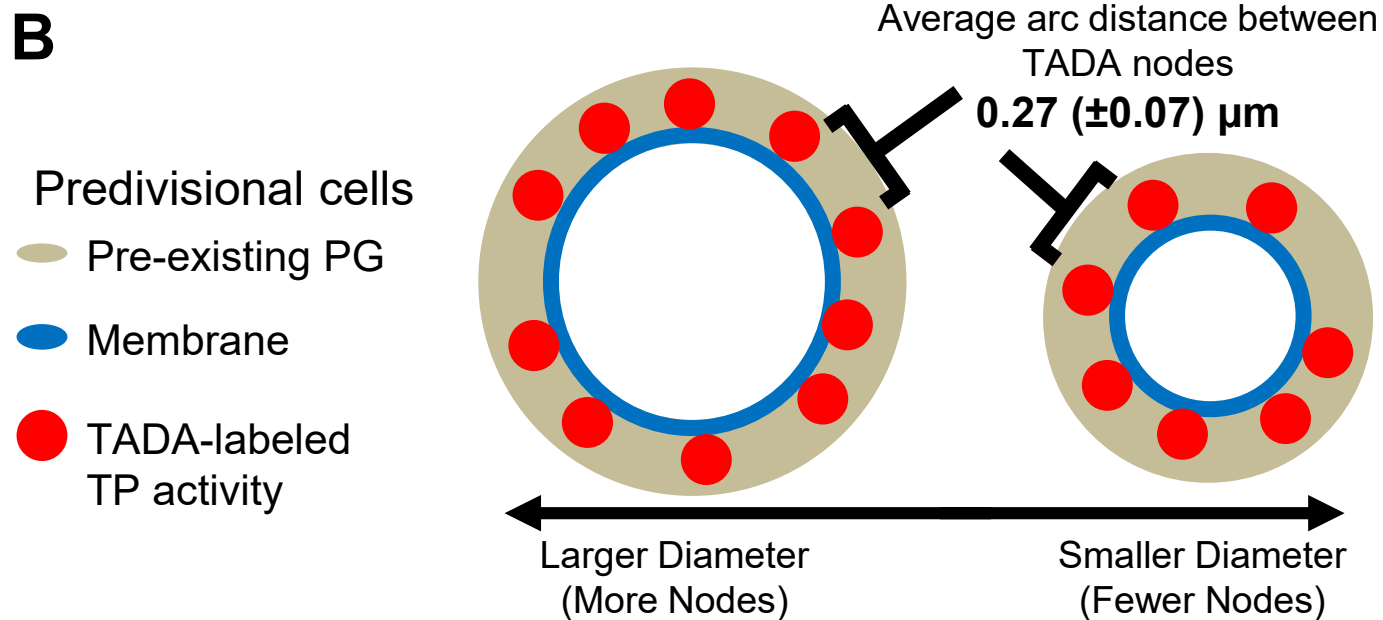
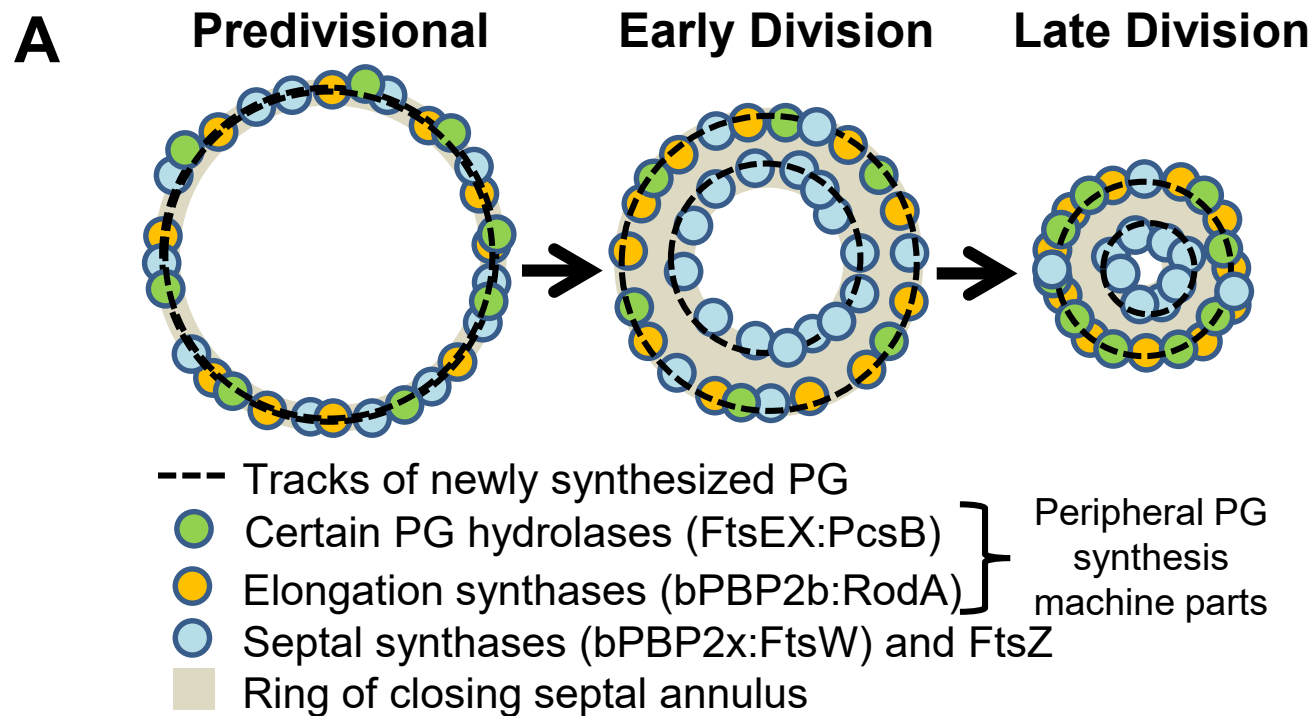


Fig. 8



**Fig. 9**